



University Of Ioannina
Physics Department



HPGe detectors characterization
and feasibility study for
cross section measurements
of neutron induced reactions on mid-weight nuclei
at INPP/NCSR “Demokritos”

M.Sc. Thesis
Peoviti Maria

Academic Supervisor: Patronis Nikolaos

Ioannina
May, 2021



Πανεπιστήμιο Ιωαννίνων
Τμήμα Φυσικής



**Χαρακτηρισμός ανιχνευτών γερμανίου υπερ-υψηλής
καθαρότητας
και μελέτη σκοπιμότητας
αντιδράσεων νετρονίων σε μεσοβαρείς πυρήνες
στις εγκαταστάσεις του ΠΣΦ του ΕΚΕΦΕ “Δημόκριτος”**

Μεταπτυχιακή Διπλωματική Εργασία
Πεοβίτη Μαρία

Ακαδημαϊκός επιβλέπων: Πατρώνης Νικόλαος

Ιωάννινα
Μάιος, 2021

Acknowledgements

First of all, I would like to express my gratitude to my supervisor Nikolas Patronis for giving me the opportunity to be a part of his team. Thank you for showing me trust and giving me guidance during this project.

Moreover, I am deeply grateful to Anastasios Lagoyannis for all the help during my stay in INPP at NCSR Demokritos, as well as Michail Axiotis for his insightful suggestions and his belief in me.

I would like to thank my colleagues, Efstathia Georgali who was more than willing to help me during this process, and Zinovia Eleme for the moments we shared. Thank you to my dear friend and colleague Elisso Stamati for the constructive conversations we had and the unwavering support.

I deeply thank my family for encouraging me to follow my dreams and supporting me to achieve my goals. Finally, thank you to my friends for their profound belief in my abilities.

Ευχαριστίες

Αρχικά, θα ήθελα να εκφράσω την ευγνωμοσύνη μου στον ακαδημαϊκό μου επιβλέποντα κ. Νικόλαο Πατρώνη, που μου έδωσε την ευκαιρία να γίνω μέλος της ομάδας του. Ευχαριστώ για την εμπιστοσύνη και την καθοδήγηση κατά τη διάρκεια αυτής της εργασίας.

Επιπλέον, είμαι βαθιά ευγνώμων στον κ. Αναστάσιο Λαγογιάννη για όλη τη βοήθεια κατά τη διάρκεια της παραμονής μου στο ΠΣΦ του ΕΚΕΦΕ Δημόκριτος, καθώς και τον κ. Μιχάλη Αξιώτη για τις προτάσεις του και την πίστη του σε μένα.

Θα ήθελα να ευχαριστήσω τις συναδέλφους μου Ευσταθία Γεωργαλή, η οποία ήταν πάντα πρόθυμη να με βοηθήσει κατά τη διάρκεια αυτής της διαδικασίας, και τη Ζηνοβία Ελεμέ για τις στιγμές που μοιραστήκαμε. Ευχαριστώ, επίσης, την καλή μου φίλη και συνάδελφο Ελισσώ Σταμάτη για τις εποικοδομητικές συζητήσεις που είχαμε και για τη συνεχή υποστήριξή της.

Οφείλω ένα μεγάλο ευχαριστώ στην οικογένειά μου που με ενθαρρύνει να ακολουθήσω τα όνειρα μου και με υποστηρίζει αδιάκοπα για την επίτευξη των στόχων μου. Τέλος, ευχαριστώ τους φίλους μου για τη βαθιά πίστη τους στις ικανότητές μου.

Abstract

In the present work, a feasibility study was performed for neutron induced reactions on mid weight nuclei, by means of the activation technique. More specifically, the study concerns the cross section measurement of the reactions $^{127}\text{I}(n,2n)^{126}\text{I}$, $^{133}\text{Cs}(n,2n)^{132}\text{Cs}$ and $^{136}\text{Ce}(n,2n)^{135}\text{Ce}$. The scope of this work is to investigate whether it is possible to conduct the specific experiments, as well as, how the experimental results can be optimized. On this respect, three CANBERRA HPGe detectors, located in the facilities of the Institute of Nuclear and Particle Physics of the National Centre of Scientific Research “Demokritos”, were characterized in terms of their efficiency.

The first step in characterizing the detectors is the experimental determination of the peak efficiency for different γ -ray energies. For this purpose, seven calibration sources were used and spectra covering a wide range of energies were acquired at six different distances from each detector. The next step, is the three dimensional modeling of the system using the simulation toolkit GEANT4 and the reproduction of the experimental data by changing the parameters of the simulation, until an agreement with the experimental data is reached.

Then, the TALYS code was utilized for the theoretical study of the cross section of the reactions. The TALYS code performs theoretical calculations of various observables on nuclear reactions. Specifically, different theoretical models were used for the study of level densities in nuclear reactions and a comparison between the theoretically calculated cross section, extracted by TALYS and the existing experimental data, was made.

The final scope of this study was the calculation of the expected counting rate for the three reactions under study, which is related to the required irradiation and measurement time of the samples. For this purpose, the results of the efficiency characterization of the detectors were utilized and the estimated future beam flux at the INPP facilities was taken into account. The calculation of the expected number of events is an essential part of any preliminary study, as it is necessary to have an estimate of the requested beam time and the measuring conditions of the induced activity.

Περίληψη

Στο πλαίσιο της παρούσας εργασίας έγινε μελέτη σκοπιμότητας μέτρησης των ενεργών διατομών των αντιδράσεων $^{127}\text{I}(n,2n)^{126}\text{I}$, $^{133}\text{Cs}(n,2n)^{132}\text{Cs}$ και $^{136}\text{Ce}(n,2n)^{135}\text{Ce}$. Συγκεκριμένα, βασικός στόχος είναι να διερευνηθεί αφενός κατά πόσο είναι εφικτή η διεξαγωγή των συγκεκριμένων πειραμάτων και αφετέρου με ποιόν τρόπο μπορούν να βελτιστοποιηθούν τα πειραματικά αποτελέσματα. Προς την κατεύθυνση αυτή, πραγματοποιήθηκε ο χαρακτηρισμός τριών ανιχνευτών γερμανίου υπερ-υψηλής καθαρότητας, οι οποίοι βρίσκονται στις εγκαταστάσεις του Ινστιτούτου Πυρηνικής και Σωματιδιακής Φυσικής του Εθνικού Κέντρου Έρευνας Φυσικών Επιστημών “Δημόκριτος”.

Το πρώτο βήμα για τον χαρακτηρισμό των ανιχνευτών είναι η λήψη πειραματικών δεδομένων, προκειμένου να προσδιοριστεί η απόδοση των ανιχνευτών. Για τον σκοπό αυτό, χρησιμοποιήθηκαν επτά βαθμονομημένες σημειακές πηγές και ελήφθησαν φάσματα σε έξι διαφορετικές αποστάσεις από το παράθυρο των ανιχνευτών. Το επόμενο βήμα ήταν η προσομοίωση του συστήματος με χρήση του υπολογιστικού πακέτου GEANT4 και η αναπαραγωγή των πειραματικών δεδομένων μεταβάλλοντας παραμέτρους της προσομοίωσης, έως ότου επιτευχθεί ικανοποιητική συμφωνία με τα πειραματικά δεδομένα.

Στη συνέχεια, για τη θεωρητική μελέτη της ενεργού διατομής των αντιδράσεων αξιοποιήθηκε ο κώδικας TALYS, προκειμένου να διερευνηθούν θεωρητικά οι παραπάνω αντιδράσεις. Συγκεκριμένα, χρησιμοποιήθηκαν διαφορετικά θεωρητικά μοντέλα για την περιγραφή των πυκνοτήτων καταστάσεων σε πυρηνικές αντιδράσεις και έγινε σύγκριση της θεωρητικά υπολογιζόμενης ενεργού διατομής που εξήχθη από το TALYS με τα ήδη υπάρχοντα πειραματικά δεδομένα.

Τελικός στόχος της εργασίας, ήταν ο υπολογισμός του αναμενόμενου αριθμού γεγονότων για τις τρεις υπό μελέτη αντιδράσεις, ο οποίος συνδέεται με τους απαιτούμενους χρόνους ακτινοβολήσης και μέτρησης των δειγμάτων. Για τον σκοπό αυτό, αξιοποιήθηκαν τα αποτελέσματα του χαρακτηρισμού απόδοσης των ανιχνευτών καθώς και η αναμενόμενη ροή νετρονίων του ΠΣΦ του Δημοκρίτου. Ο υπολογισμός της αναμενόμενης στατιστικής αποτελεί ένα σημαντικό τμήμα του σχεδιασμού μελλοντικών πειραμάτων, καθώς είναι απαραίτητο να υπάρχει ακριβής γνώση του ζητούμενου χρόνου δέσμευσης του επιταχυντή, καθώς και για τον καθορισμό των συνθηκών μέτρησης της επαγόμενης ακτινοβολίας γ .

Contents

Acknowledgements

Ευχαριστίες

Abstract

Περίληψη

1. Introduction.....	1
1.1 Motivation.....	2
1.2 Previous experimental data of the three neutron induced reactions.....	3
1.3 Nuclear reaction mechanisms.....	4
1.4 The Activation technique.....	6
1.5 HPGe detectors and γ spectroscopy.....	7
1.5.1 Interaction of photons with matter.....	7
1.5.2 Band structure in solids.....	10
1.5.3 Semi-conductor detectors.....	12
1.5.4 High Purity Germanium detectors (HPGe).....	12
2. HPGe detectors characterization.....	15
2.1 Efficiency measurements.....	16
2.1.1 Experimental setup.....	16
2.1.2 Data analysis.....	19
2.1.3 Experimental efficiency and resolution.....	20
2.2 Simulation.....	23
2.2.1 GEANT4.....	23
2.2.2 Efficiency characterization.....	24
3. Theoretical calculations.....	29
3.1 The TALYS code.....	30

3.1.1 Cross section calculations for compound nucleus reactions.....	31
3.1.2 Level densities.....	32
3.2 TALYS calculations	35
3.2.1 Excitation function of the reaction $^{127}\text{I}(n,2n)^{126}\text{I}$	35
3.2.2 Excitation function of the reaction $^{133}\text{Cs}(n,2n)^{132}\text{Cs}$	36
3.2.3 Excitation function of the reaction $^{136}\text{Ce}(n,2n)^{135}\text{Ce}$	37
4. Expected Counting rates.....	38
4.1 Tandem Accelerator facility.....	39
4.2 Energy diagrams of the reactions.....	40
4.3 Expected counting rates.....	42
4.3.1 Expected counting rate for the reaction $^{127}\text{I}(n,2n)^{126}\text{I}$	43
4.3.2 Expected counting rate for the reaction $^{133}\text{Cs}(n,2n)^{132}\text{Cs}$	44
4.3.3 Expected counting rate for the reaction $^{136}\text{Ce}(n,2n)^{135}\text{Ce}$	46
5. Conclusions.....	47
5.1 Conclusions.....	48
References.....	50
Appendix A.....	53
Appendix B.....	65
Appendix C.....	67

Chapter 1 - Introduction

1.1 Motivation

The aim of this work is to investigate the feasibility of three neutron induced reactions at the Institute of Nuclear and Particle Physics (INPP) at the National Centre of Scientific Research (NCSR) “Demokritos” [1].

The study of nuclear reactions remains an open field of research, with one of its primary goals being the study of nuclear reactions’ cross sections. The study of the reactions’ cross sections, both experimentally and theoretically, and the subsequent comparison of the two types of results, can provide an insight on the nuclear reaction models and nuclear structure. As a result, many existing applications can be improved and new ones can be developed in the future.

The study of neutron induced reactions’ cross sections is important in several applications and fields such as astrophysics, dosimetry, radiation therapy, medical applications, reactors and accelerator-driven subcritical systems (ADS). Experimental data on neutron induced reactions are also important for fusion and fission projects. They are used for calculations on nuclear heating, nuclear transmutation rates, induced radioactivity, as well as, radiation damage effects. More specifically, cerium is used in many new applications, such as in the glass industry, as a hardening agent and in nuclear fuels, as diluent in uranium, plutonium and thorium oxide due to its low neutron capture cross section. Concerning the $^{133}\text{Cs}(n,2n)^{132}\text{Cs}$ reaction, the ^{133}Cs isotope is evaluated to have large fission yield. Thus, the cross sections of those neutron induced reactions are of interest and it is important to be measured with improved uncertainties [2-5].

In addition to all its applications, the investigation of the experimental cross sections is valuable in the process of testing and improving various theoretical models. In many physics cases, the experimental data and the theoretical calculations differ greatly. Furthermore, inconsistency is observed between the existing experimental results. Specifically, for the $^{136}\text{Ce}(n,2n)^{135}\text{Ce}$ physics case, according to our previous findings on (n,2n) reactions on stable -but neutron deficient- isotopes, it was a strong evidence that the GSM level density model fails with respect to the reproduction of the experimental data [6-8]. For this reason we consider the experimental and theoretical investigation of this reaction is of special interest.

The feasibility study of the aforementioned experimental campaigns had to be contacted in the light of the new abilities of the Tandem Accelerator Laboratory of the INPP after the accelerator upgrade activities and considering also the three new and recently acquired HPGe detectors. These two axes of upgrade provided new abilities for activation measurements that were previously not achievable.

1.2 Previous experimental data of the three neutron induced reactions

As can be seen in Fig. 1.2.1 the $^{127}\text{I}(n,2n)^{126}\text{I}$ reaction cross section has been measured from several groups so far, but the existing data are not consistent.

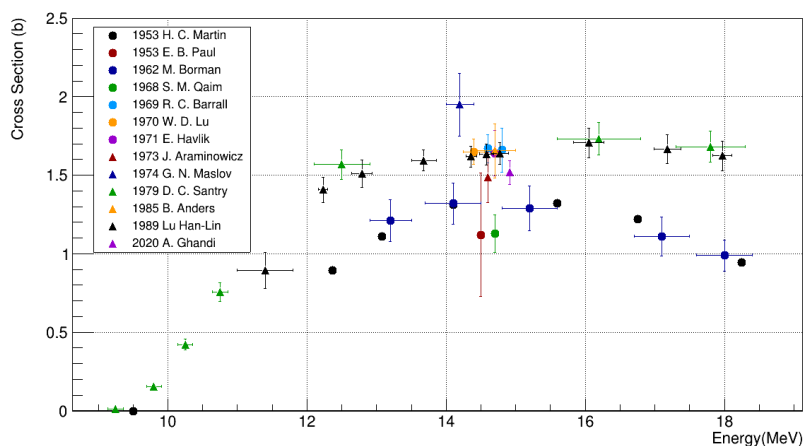


Figure 1.2.1: The $^{127}\text{I}(n,2n)^{126}\text{I}$ reaction existing experimental cross section data as obtained from the EXFOR database [9].

Concerning the reaction $^{133}\text{Cs}(n,2n)^{132}\text{Cs}$, the experimental data are fewer and cover a narrower energy range.

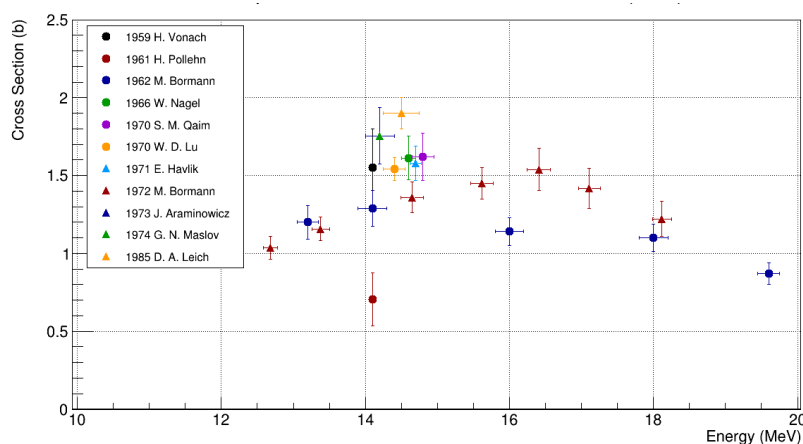


Figure 1.2.2: The $^{133}\text{Cs}(n,2n)^{132}\text{Cs}$ reaction existing experimental cross section data as obtained from the EXFOR database [9].

As can be seen in Fig. 1.2.2 the existing experimental data are discrepant. Also, there is a lack of experimental information at near threshold energies.

Finally, concerning the reaction $^{136}\text{Ce}(n,2n)^{135}\text{Ce}$, as can be seen in Fig. 1.2.3 only a few experimental studies have been performed so far and all of them are limited in the energy range between 13-15 MeV. There are no data at low, near threshold energies, neither on the higher neutron beam energies -close to the onset of the (n,3n) reaction channel.

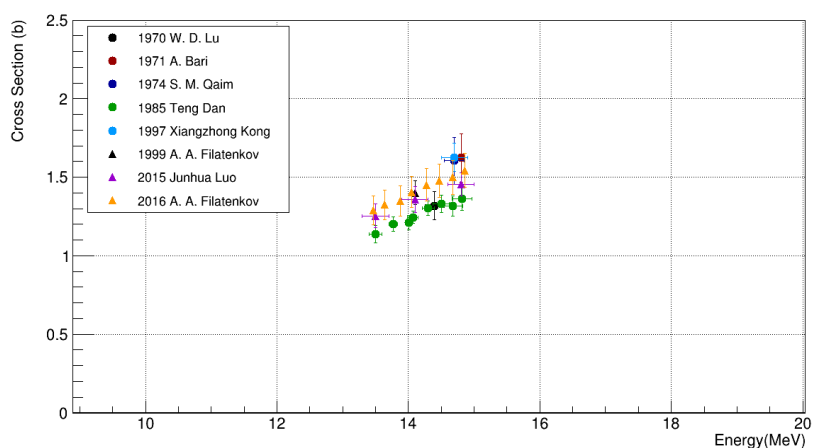


Figure 1.2.3: The $^{136}\text{Ce}(n,2n)^{135}\text{Ce}$ reaction existing experimental cross section data as obtained from the EXFOR database [9].

The aforementioned physics cases, show significant discrepancies between the existing experimental data, as well as, an obvious lack of them in a wide range of energies. Thus, further experimental data must be obtained in order to provide solid constrains on theoretical calculations and their parameterization.

Within the present work, the feasibility study of the reaction cross section measurements given in the Table 1.2.1 is presented.

Reaction	Neutron energy (MeV)	Previous experimental data
$^{127}\text{I}(n,2n)^{126}\text{I}$	17, 18, 19	some (discrepant)
$^{133}\text{Cs}(n,2n)^{132}\text{Cs}$	10.1, 10.4, 10.7	none
	17, 18, 19	some
$^{136}\text{Ce}(n,2n)^{135}\text{Ce}$	17, 18, 19	none

Table 1.2.1: Proposed measurements for each reaction.

1.3 Nuclear reaction mechanisms

A typical nuclear reaction is written as:

$$a + A \rightarrow a' + A' \quad \text{or in a more compact form} \quad A(a, a')A'$$

where:

a: projectile

A: target (usually stationary in the laboratory)

a': ejectile

A' : residual nucleus

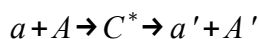
All nuclear reactions can be classified into two major categories:

- Direct reactions
- Compound nucleus reactions

In a direct reaction, the projectile interacts primarily with the nucleons on the surface of the target. Direct reactions take place over a short period of time (10^{-22} s), which is not enough to cause the projectile to lose its entire energy. In this category, there exist four subcategories:

1. Elastic scattering: no nucleons are exchanged between the projectile and the target. Only the kinetic energy and the momentum change after the reaction.
2. Inelastic scattering: no nucleons are exchanged. Part of the kinetic energy is converted into excitation energy of the interacting nuclei.
3. Stripping reactions: transfer of nucleons from the projectile to the target.
4. Pick up reactions: transfer of nucleons from the target to the projectile.

Concerning the compound nucleus reactions, the projectile interacts with the whole nucleus. This type of reactions require more time ($10^{-16} - 10^{-18}$ s) and the projectile's energy is distributed among all the nucleons of the target, until the system reaches a thermodynamic equilibrium. The projectile is completely absorbed by the target resulting in the creation of the compound nucleus. Regarding the formalism, a compound nucleus reaction is written as:



The compound nucleus is formed at an excited state and then de-excites emitting one or more particles and creating the residual nucleus. This happens in a way that is independent of the input channel, leading to the principle called Bohr Independence hypothesis. This hypothesis states that the compound nucleus may decay through different ways. The decay mechanism is independent of the mechanism that caused the formation of the compound nucleus.

There is an additional category of nuclear reactions that take place at intermediate time scales. These are the pre-equilibrium reactions, which, as their name suggests, occur when a particle gains enough energy to escape before the equilibrium is reached. In this case, the input and output channels are not completely independent.

The reaction mechanism that will prevail largely depends on the kinetic energy of the projectile. The compound nucleus mechanism is predominant for relatively low incident energies (10 – 20 MeV). Low energy corresponds to large de Broglie wavelength, which allows the projectile to interact with the whole target nucleus and form the compound nucleus. On the contrary, high energies result to small de Broglie wavelengths, which limits the interaction range between the projectile and the target to the surface, thus making the direct reactions dominant. The pre-equilibrium mechanism takes place in between the two extremes [10-12].

The cross section of each mechanism according to the reaction time and energy is shown in Figure 1.3.1.

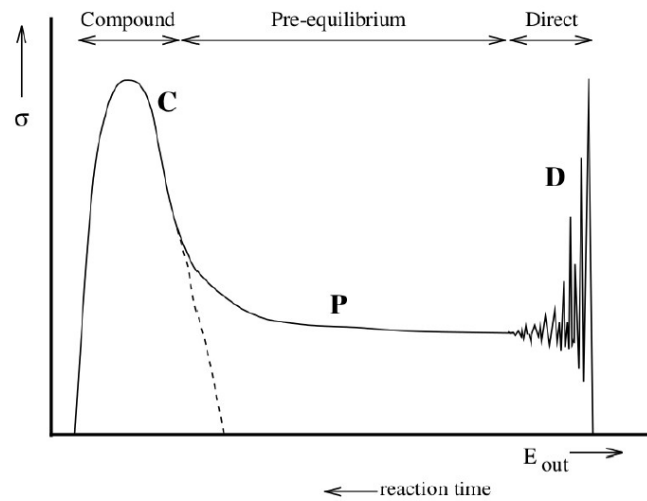


Figure 1.3.1: Schematic representation of the predominant regions of the three mechanisms according to energy and time [12].

1.4 The Activation technique

The Activation Technique is widely used for the determination of the cross section of nuclear reactions. This method consists of two stages:

1. The sample is irradiated by a particle beam and the unstable product nuclei are formed.
2. The induced activity in the irradiated samples is measured.

The cross section of the reaction can be obtained using the formula:

$$\sigma = \frac{\text{counts} \cdot CF}{N_T \cdot \Phi \cdot \varepsilon \cdot I_\gamma \cdot (1 - e^{-\lambda t_m}) \cdot e^{-\lambda t_w} \cdot f_B}$$

where:

counts: number of counts recorded

CF: correction factors which include self attenuation corrections, coincidence summing effects corrections, dead time corrections

N_T : the number of stable nuclei in the irradiation sample

Φ : irradiation flux

ε : efficiency of the detector for the emitted radiation

I_γ : the intensity of the emitted γ -ray

λ : decay constant of the daughter nucleus

t_m : measuring time of the induced activity

t_w : waiting time between the end of the irradiation and the start of the measurement

f_B : correction factor for the activated nuclei decay during the irradiation, where

$$f_B = \frac{(1 - e^{-\lambda t_{irr}})}{\lambda t_{irr}} \quad \text{for constant flux}$$

$$f_B = \frac{\int_0^{t_{irr}} f(t) e^{\lambda t} dt}{\int_0^{t_{irr}} f(t) dt} \quad \text{for non constant flux}$$

$f(t)$: beam flux at a certain moment t

t_{irr} : total time of the irradiation

There is a variety of factors that need to be taken into account before proceeding with the application of this method. These are related to the counting rate of the measurements, the purity of the recorded spectrum, as well as, possible contamination from interfering reactions. The study of the above is the main goal of the feasibility study of the experiment.

Firstly, the daughter nucleus must have a long enough half-life to ensure that the nuclei will not decay during the waiting time, before the activity measurement takes place. However, the half life cannot be too long, otherwise the emission rates will be too slow. In such cases, the irradiation and measuring times necessary to obtain adequate statistics will have to increase significantly. Furthermore, the intensity of the emitted radiation plays an important role, as γ -rays with very low intensities (<1%) cannot be detected.

An important part of the feasibility study of an experiment concerns the interference of other reactions. It is crucial that no reactions produce the same isotope as the one being populated by the reaction of interest. The probability of this phenomenon increases as the number of isotopes present in the sample increases. A similar problem occurs when other nuclear reactions result in the emission of radiation with energy close enough to the decay energy of interest. During the preliminary study, it has to be ensured that the final spectrum will be as pure as possible and no possible contamination can influence the results. Otherwise, an investigation must be carried out on how those phenomena can be corrected [6].

1.5 HPGe detectors and γ spectroscopy

The detection of any type of particle or radiation is based on the collection of secondary particles and the recording of the produced electrical signal. Secondary particles are produced in different ways, depending on whether it is particles or radiation that interact with the detection material. Charged particles produce a signal within a detector by ionization and excitation of the detector material directly. Radiation, on the other hand, is uncharged and consequently, its detection is based on different mechanisms.

1.5.1 Interaction of photons with matter

A large number of possible interaction mechanisms between γ -rays and matter is known, but only three types play a significant role in radiation measurements. Those are the photoelectric

absorption, Compton scattering and pair production. All these processes lead to the partial or complete transfer of the γ -ray energy to an electron. Free electrons are produced and, as these electrons are slowed down while moving through matter, they create electron-hole pairs inside the detector's material.

Photoelectric Effect

In the photoelectric effect, the incident photon interacts with the atom as a whole. All of the photon energy is absorbed and as a result an energetic photoelectron is ejected from the atom.

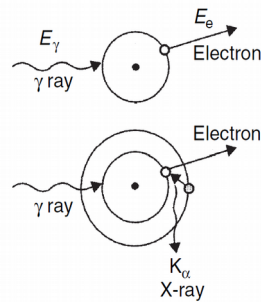


Figure 1.5.1.1: A schematic representation of the photoelectric effect [14].

After the absorption of the photon, the atom is left in an excited state and in order to recover its equilibrium, the atom may de-excite by distributing the excitation energy between its remaining electrons, or by filling the vacancy with a higher energy electron. This is accomplished with the emission of a characteristic x-ray [13-16].

Compton Scattering

The process of Compton scattering takes place between the incident γ -ray and an electron in the absorbing material. The incoming γ -ray is deflected through an angle with respect to its original direction and transfers a portion of its energy to the recoil electron.

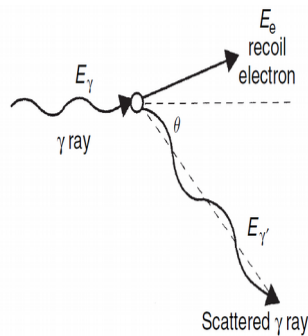


Figure 1.5.1.2: A schematic representation of the Compton scattering process [14].

All angles of scattering are possible, thus the energy transferred to the electron can vary from zero to a large fraction of the γ -ray energy. From the conservation of energy and momentum, the energies of the outgoing photon and electron are related to the angles at which they are emitted. The formula that gives the energy of the scattered photon is:

$$E'_\gamma = \frac{E_\gamma}{1 + \frac{E_\gamma}{m_0 c^2} (1 - \cos\theta)}$$

where:

$m_0 c^2 = 511 \text{ keV}$: the rest mass energy of the electron [13-16].

Pair Production

Pair production results in the conversion of a photon into an electron-positron pair. The process of pair production is energetically possible if the incident photon energy exceeds twice the rest mass energy of an electron ($E_\gamma > 1.02 \text{ MeV}$), however it becomes predominant as the photon energy increases above several MeV. All the excess energy above the 1.02 MeV, goes into kinetic energy shared by the positron and the electron.

The positron will interact with an electron and annihilate and, as a result, two annihilation photons, with energies of 511 keV, are produced. The kinetic energy of the electron-positron pair will be absorbed instantly, but each 511 keV photon will carry its energy to another location where it will interact further by Compton scattering or photoelectric absorption with the electrons in the medium [13-16].

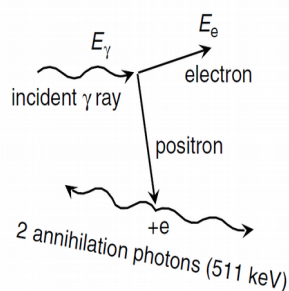


Figure 1.5.1.3: A schematic representation of the pair production process [14].

The photon energy range at which each interaction mechanism is predominant is illustrated in Figure 1.5.1.4.

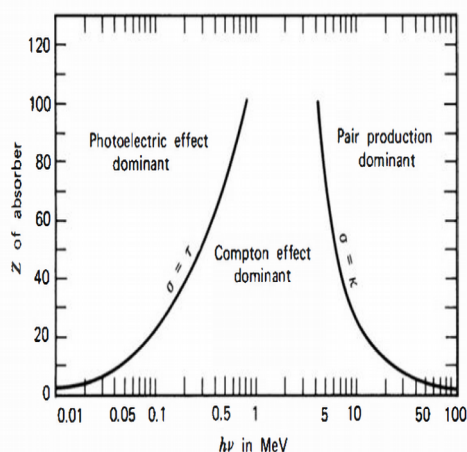


Figure 1.5.1.4: The predominant photon interaction mechanisms with regards to their energy [13].

1.5.2 Band structure in solids

In a free atom, the electrons are placed in precisely determined energy levels. Combining a collection of atoms together into a solid structure, broadens them into regions of many discrete levels so closely spaced, that they can be considered a continuum, each of which can contain a fixed number of electrons. Those continuous regions are separated by a forbidden energy region or a gap.

The lowest energy band, is known as the valence band and corresponds to the outermost shell electrons. Lying above the valence band, is the conduction band and it contains the electrons that are fully detached from their atoms and hence are free to move inside the crystal lattice. Electrons in this band contribute to the electrical conductivity of the material. These two bands are separated by the band gap, the size of which is used to classify the material as a conductor, semiconductor or an insulator.

A conductor has a non-existent band gap, thus it is always characterized by high electrical conductivity. On the other hand, insulators and semi-conductors have a finite value of a band gap. In their case, the electrons must have enough energy to cross the band gap and reach the conduction band in order for the material to exhibit conductivity. For insulators, the band gap is typically of the order of 10 eV, while for semi-conductors it is much lower. The classification of solids according to their band gaps is illustrated in Figure 1.5.2.1.

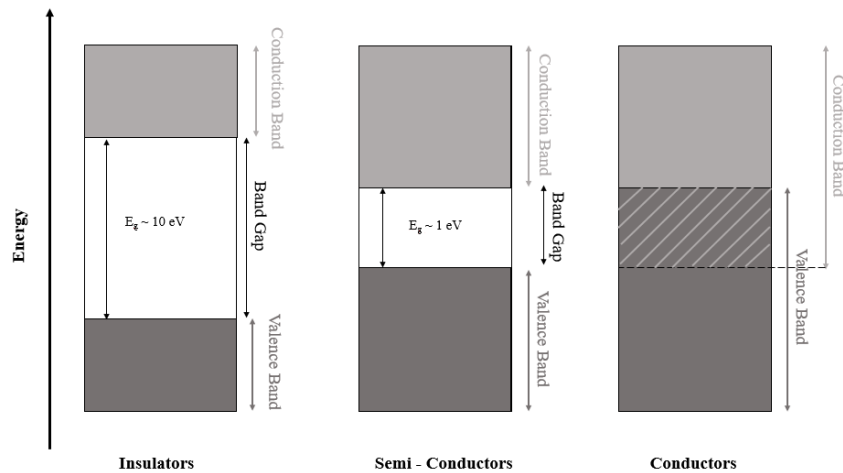


Figure 1.5.2.1: The band structure in solids.

If a valence electron gains sufficient energy it can cross the band gap and reach the conduction band. The excitation process creates an electron in the otherwise empty conduction band and it leaves a vacancy in the valence band, referred to as a hole. Both the electron and the hole will move in opposite directions throughout the crystal if an external electric field is applied. Since both electrons and holes carry charge, the conductivity of the material is a result of the motion of both of them.

At any nonzero temperature, there is some amount of thermal energy that is shared by the electrons in the crystal lattice. Consequently, there is a probability that an electron-hole pair is thermally generated and this probability is given by the following formula

$$p(T) = CT^{3/2} e^{\frac{-E_g}{2kT}}$$

where:

C: proportionality constant depending on the material

T: the absolute temperature

k: is the Boltzmann constant

E_g : the material's band gap energy

If the bandgap of the material is as low as several eV, the material will have high enough conductivity due to thermal excitation for it to be classified as a semiconductor.

The most commonly used semi-conducting materials are Si and Ge, with a bandgap of ~1 eV [13-16].

1.5.3 Semi-conductor detectors

One element that plays a significant role in the conductivity of a semiconductor is the number of impurities. An impurity is an atom of different valency which replaces an atom in the lattice and thus disturbs its electronic balance. If the impurity is a lower valent atom it results in a hole. Such impurities can be acceptor impurities. In this case the material is referred to as a p-type, where 'p' stands for positive acceptor impurities. These impurities, when distributed throughout the semiconductor material give rise to extra energy states just above the valence band. On the other hand, when an atom of higher valency than the lattice, is introduced, it provides an extra electron. In this case, a donor impurity is created, that causes the formation of states just below the conduction band. Such a material is called n-type, where 'n' stands for negative donor impurities.

When bringing those two materials in contact, a junction or a diode is created. Holes may begin to stray from the p side to the n side of the junction capturing electrons from the n side to the p side filling up holes in the process. As a result, a region will appear, where the excess charge carriers have canceled each other out. This region is called depletion region.

In order for the junction to properly operate as a detector, a suitable external voltage must be applied causing the semiconductor diode to be reversed biased. The p-n junction is the most broadly used diode. When reverse bias is applied, the thickness of the depletion region is increased, extending the volume over which charge carriers, produced by the incident radiation, will be collected.

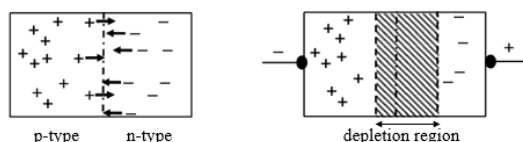


Figure 1.5.3.1: A junction (left) and the creation of the depletion region due to diffusion (right) [14].

When ionizing radiation enters the depletion region, it creates electron-hole pairs in the material, which are then swept out by the electric field. By adding electrical contacts on the ends of the junction, the collection of these charge carriers is possible, resulting in a signal proportional to the energy of the incident particle. This is the principle of operation of semiconductors as detectors. The depletion region is the region of the junction from where carriers corresponding to interactions can be collected and studied, and thus is called the active volume of the detector [13-16].

1.5.4 High Purity Germanium detectors (HPGe)

Considering that γ radiation is highly penetrating, the active volume of the detector has to be large enough in order for photons to be able to deposit all their energy in it. For a simple junction, the thickness of the depletion region is given by:

$$d = \sqrt{\frac{2 \epsilon V}{eN}}$$

where:

ϵ : the dielectric constant

V : the reverse bias voltage

e : the electron charge and

N : the net impurity concentration of the material.

In order to increase the depletion depth for a given bias voltage, the impurity concentration must be reduced. This can be achieved with techniques that reduce the impurities to 10^{10} atoms/cm³ resulting in a High Purity Germanium detector, or simply HPGe detector.

Germanium, which is one of the most commonly used semiconductors for the creation of γ -ray detectors, has a band gap of 0.7 eV. This gives rise to a large leakage current which is caused by thermal electron-hole pair creation in the depletion region. This current results in an unacceptable noise and therefore a germanium detector must be cooled to liquid nitrogen temperature (i.e. 77.2 K) during its operation.

The high purity crystal is the active volume of the detector. On top of the crystal, impurity atoms are implanted or diffused, creating electrically conducting surfaces where an external voltage is applied. If the impurities are donor atoms they form the n⁺ contact, also referred to as the positive electrode, whereas if the impurities are acceptor atoms they form the p⁺ contact, which is the negative electrode. These contacts produce an insensitive layer of attenuated material, from which the charge carriers are not collected and are therefore called dead layers of the detector [13-16].

Energy Resolution

One of the two main quantities of interest when using any detection system is its energy resolution. The resolution provides an estimate of how well the detector can distinguish two energy peaks lying close to each other. If two peaks lie closer than the FWHM (Full Width at Half Maximum) they cannot be distinguished. At a given energy E , the resolution is given by:

$$R = \frac{FWHM}{E}$$

A characteristic of HPGe detectors is their good energy resolution, as a spectrum recorded by an HPGe will present sharp peaks [13-16].

Detection efficiency

The second quantity that is significant in spectroscopy is the detection efficiency, which depends primarily on the size and shape of the detector.

When it comes to efficiency, one usually refers to the photopeak efficiency, which differs from the total efficiency. The first is connected to the number of photons whose energy was

recorded in the photopeak, while the second is connected to the number of photons that deposited any amount of energy in the crystal.

The photopeak efficiency is divided into two categories. The absolute efficiency is given by:

$$\varepsilon_{ab} = \frac{\text{events recorded by the detector}}{\text{total emissions by the source}}$$

Whereas, the intrinsic efficiency is given by:

$$\varepsilon_{intr} = \frac{\text{events recorded by the detector}}{\text{events incident on the detector}}$$

The absolute efficiency depends on the geometrical configuration of the set up, as well as, the size and shape of the detector. The absolute efficiency is proportional to the intrinsic efficiency by a factor G:

$$\varepsilon_{ab} = \varepsilon_{intr} \cdot G$$

where:

$$G = \frac{\Delta\Omega}{4\pi}$$

$\Delta\Omega$: the solid angle the detector covers [13-16].

◆ Chapter 2 – HPGe detectors characterization ◆

2.1 Efficiency measurements

The experimental data used in this work, were obtained at the facilities of the Institute of Nuclear and Particle Physics at the National Centre of Scientific Research “Demokritos”.

2.1.1 Experimental setup

Seven point sources were measured by three identical n-type coaxial CANBERRA HPGe detectors (model : GR8023) with carbon epoxy window, at six different source-to-detector distances. The detectors are presented in Figure 2.1.1. The serial numbers of the detectors are: 16522 , 21506, and 21504.



Figure 2.1.1: The three CANBERRA HPGe detectors.

The sources utilized for the characterization are part of a calibration set by Eckert and Ziegler. Figure 2.1.2 shows a ^{152}Eu source that is part of this set.



Figure 2.1.2: The ^{152}Eu source from the Eckert and Ziegler calibration gamma set.

Table 2.1.1 contains the sources' specifications.

Isotope	A_{ref} (kBq)	$\sigma_{A_{\text{ref}}}$ (kBq)	Reference date
^{152}Eu	3.992	0.144	01-01-2015
^{137}Cs	38.15	1.37	01-01-2015
^{54}Mn	37.89	1.36	01-01-2015
^{133}Ba	36.43	1.31	01-01-2015
^{22}Na	37.59	1.35	01-01-2015
^{60}Co	33.47	1.20	01-01-2015
^{109}Cd	37.11	1.34	01-01-2015

Table 2.1.1: The specifications of the sources used in this work.

The most widely used calibration source is ^{152}Eu . It is known for emitting a variety of different γ -rays in a broad energy range (121 – 1408 keV). However, intricate decay schemes like this, can lead to summing effects when a close detection geometry is adopted.

True coincidence summing occurs when two γ -rays, or a γ -ray and an x-ray are emitted simultaneously from the nucleus. This usually involves an isotope that emits multiple cascade γ -rays in its decay, such as ^{152}Eu . The detection system records the sum of the coincident rays' energy, resulting in loss of counts from the individual full-energy peaks, ultimately leading to a loss of efficiency. This phenomenon is more intense in close detection geometries due to the increase of the solid angle [13-14]. In order to avoid inaccuracies due to summing effects in the construction of the efficiency curves, monoenergetic radioactive sources were employed as well. The measurements were performed at six source-to-detector distances, that range from 2.7 cm up to 21.8 cm.

In order to obtain spectra for different source-to-detector distances, a base with a moving part was used. The base remained fixed on the workbench and had two metal rails, along which, a "wagon" was free to move. Supported on the wagon lied the source holder which was placed at a suitable height, so that the source, which was placed vertically, was centered relative to the detector by means of a laser caliber. Figure 2.1.3 shows a graphical representation of the experimental set up.

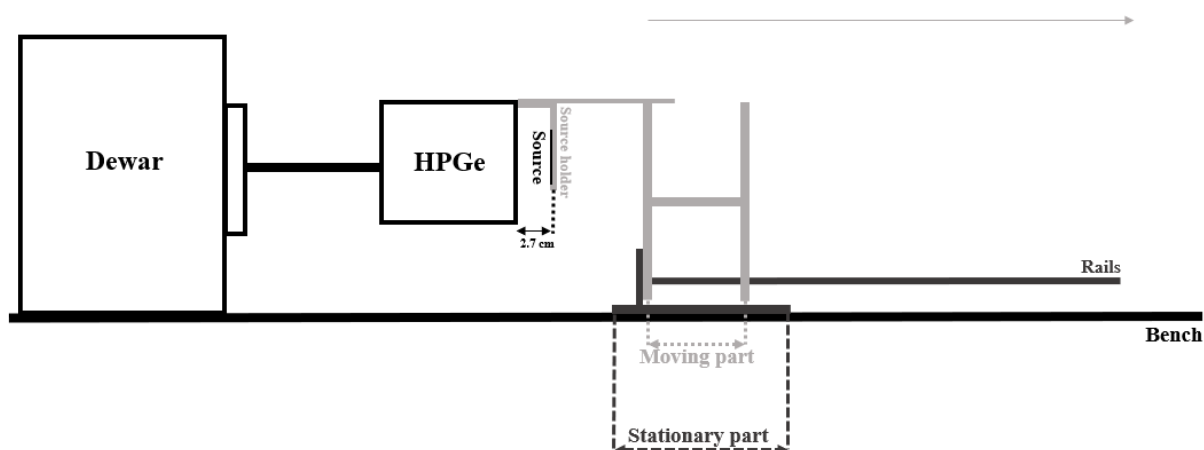


Figure 2.1.3: The graphical representation of the experimental set up (side view).

As shown in Figure 2.1.3, the minimum achievable source-to-detector distance was at 2.7 cm due to the shape of the sample holder. On the other hand, the rails on which the wagon was moving, were long enough to provide distances of up to 30 cm.

In order to accurately characterize a detector, it is crucial to obtain experimental data at a wide range of energy and different source-to-detector distances. Table 2.1.2 summarizes the isotopes used, the measured γ -rays, as well as the source-to-detector distance that every isotope was measured.

Isotope	E_γ (keV)	SD Distances (cm)					
		2.7	5	7.1	12	17	21.8
^{109}Cd	88.0336	2.7	5	7.1			
^{152}Eu	121.7817	2.7	5	7.1	12	17	21.8
	244.6974						
	344.2785						
	443.9606						
	778.9045						
	964.057						
	1112.076						
1408.013							
^{133}Ba	80.9979				12	17	21.8
	276.3989						
	302.8508						
	356.0129						
^{137}Cs	661.657				12	17	21.8

^{54}Mn	834.848	2.7	5	7.1	12	17	21.8
^{60}Co	1173.228 1332.492				12	17	21.8
^{22}Na	1274.537			7.1	12	17	21.8

Table 2.1.2: The sources measured in this work along with the γ ray energies and the source – detector distances that the measurements were carried out.

Along with all the aforementioned measurements, a background spectrum was obtained at the facilities of INPP in order to be later inspected and it is presented in Figure 2.1.4 below.

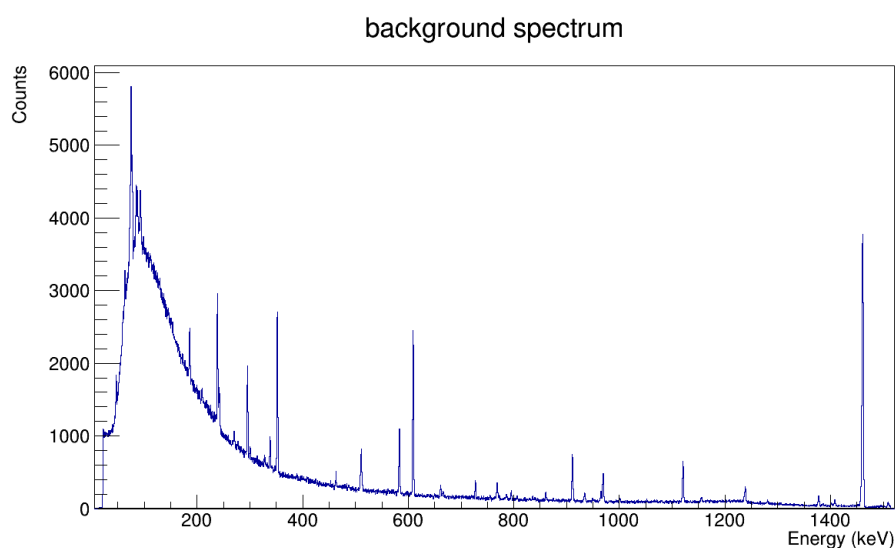


Figure 2.1.4: The background spectrum of the Tandem accelerator facility.

2.1.2 Data analysis

The data analysis in this work was performed using ROOT. ROOT is an object oriented framework developed and used by CERN (Conseil Européen pour la Recherche Nucléaire). It is widely used in many scientific fields, mainly high energy and nuclear physics, as well as medicine and industry. It is based on the C++ programming language but can also be used in other languages, such as Python.

The user can process and analyze data by creating graphs, histograms, functions, etc. and perform statistical analysis on them, as well as visualize the simulation. ROOT also offers the possibility to store data in forms that are easily accessible and inspected and do not take up much space, called ROOT "trees"[17].

Figure 2.1.2.1 shows a spectrum of a ^{152}Eu source at 21.8 cm, obtained by one of the three detectors, plotted using ROOT.

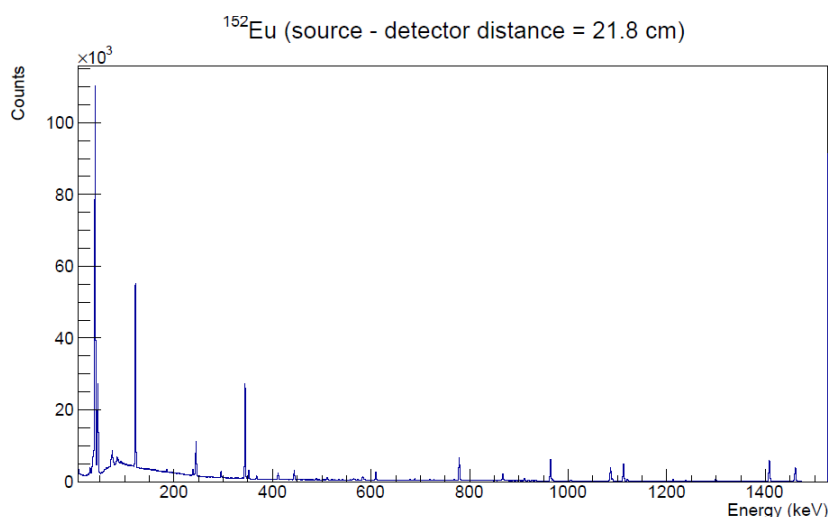


Figure 2.1.2.1: A spectrum of a ^{152}Eu source.

2.1.3 Experimental efficiency and resolution

Figure 2.1.2.1 shows two photopeaks at the low energy part of the spectrum, corresponding to the x-rays of ^{152}Eu (~40 keV). This is directly related to the material of the window of the detector, which in this case is a very thin layer (0.5 mm) of carbon epoxy, that allows the low energy photons to pass through it, reach the crystal and be recorded by the detector. During the experimental data acquisition process, the minimum energy the detectors were able to record was at ~25 keV, which correspond to the x-rays of the ^{109}Cd source. Concerning the energy resolution, it was found to be less than 2.7 keV at the reference energy of 1332 keV photons from ^{60}Co , for each of the three detectors.

The detection efficiency is calculated via:

$$\text{efficiency} = \frac{\text{counts}}{\text{emissions}} = \frac{\text{counts}}{A(\text{Bq}) \cdot I_{\gamma} \cdot \text{live time}(s)}$$

where:

counts: net area of the photopeak

A: activity of the source at the time of the measurement

I_{γ} : intensity of the γ -ray

live time: the duration of the measurement

Figure 2.1.3.1 shows an example of the full energy peak efficiency against the energy, for one of the three detectors.

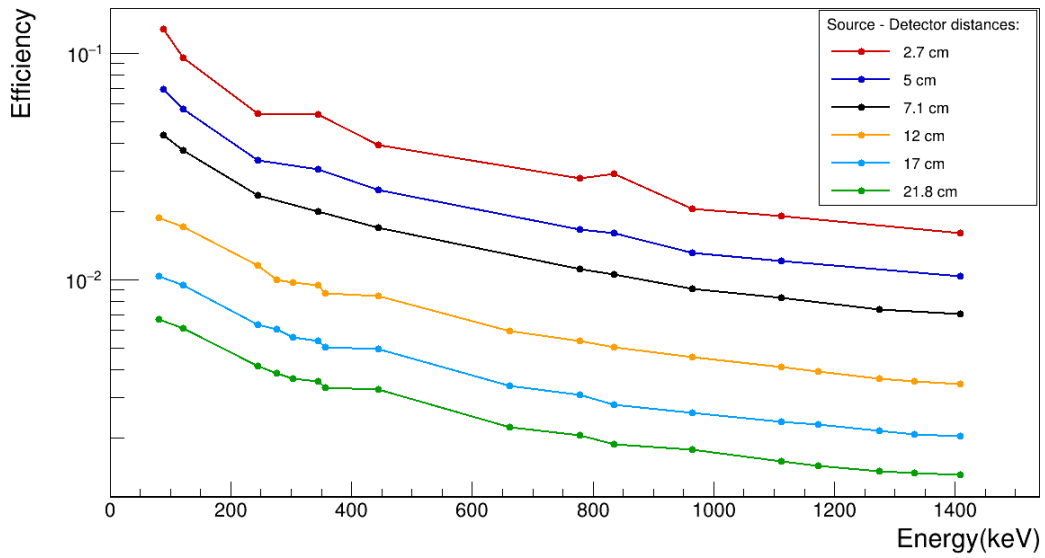


Figure 2.1.3.1: The efficiency curves for different source detector distances.

The efficiency of the detector decreases as the photon energy increases and, as well as, the source-to-detector distance increases. The three detectors are similar in size and their efficiency does not differ significantly. Figure 2.1.3.2 shows a comparison of the efficiency of all three detectors.

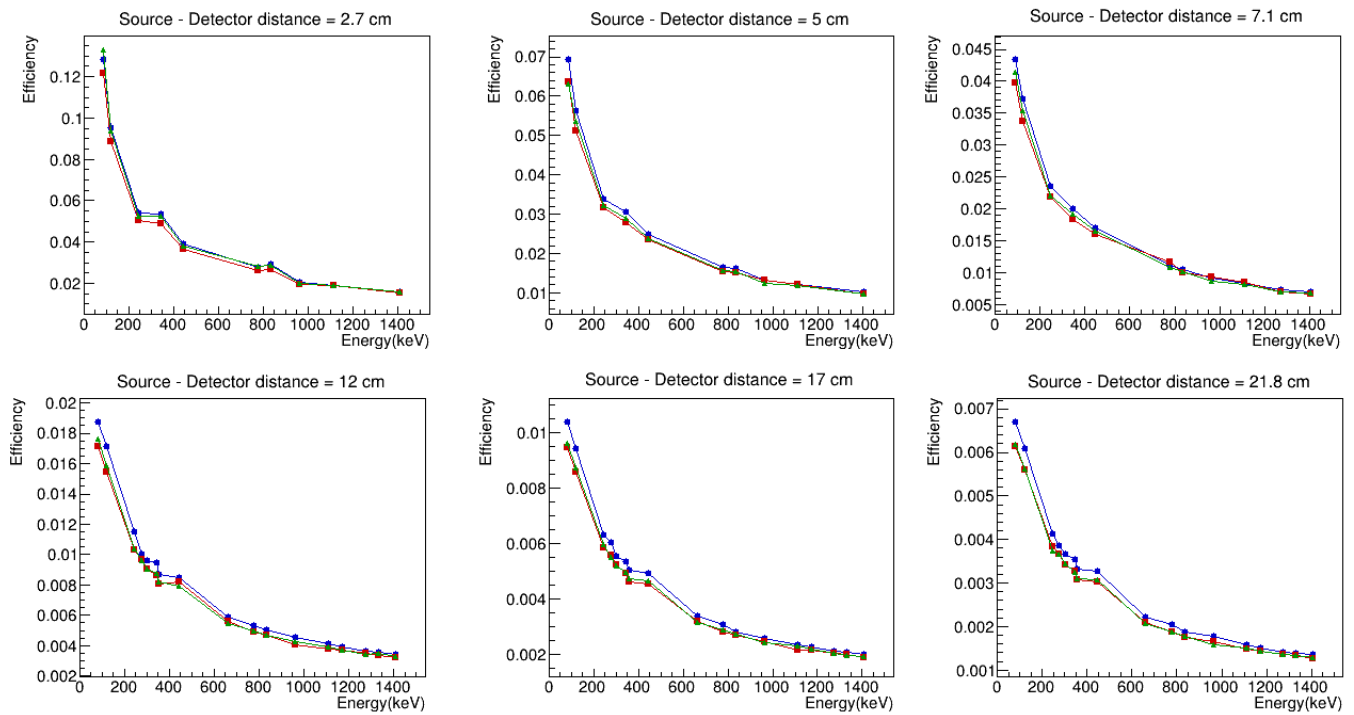


Figure 2.1.3.2: A comparison for the efficiency of the three detectors.

One of the three detectors is consistently more efficient at every distance, due to the fact that it possesses a slightly larger crystal than the other two. The dimensions of the three crystals are listed on the table below.

	Detector 1 (S/N: 21506)	Detector 2 (S/N: 21504)	Detector 3 (S/N: 16522)
Crystal Diameter (mm)	74.9 ± 0.2	75.0 ± 0.2	78.0 ± 0.2
Crystal Length (mm)	74.5 ± 0.3	74.9 ± 0.3	71.8 ± 0.3

Table 2.1.3.1: The dimensions of the crystals of the three detectors.

The next step involves the fitting of the experimental data using different fitting functions. An example is shown in Figure 2.1.3.3 below.

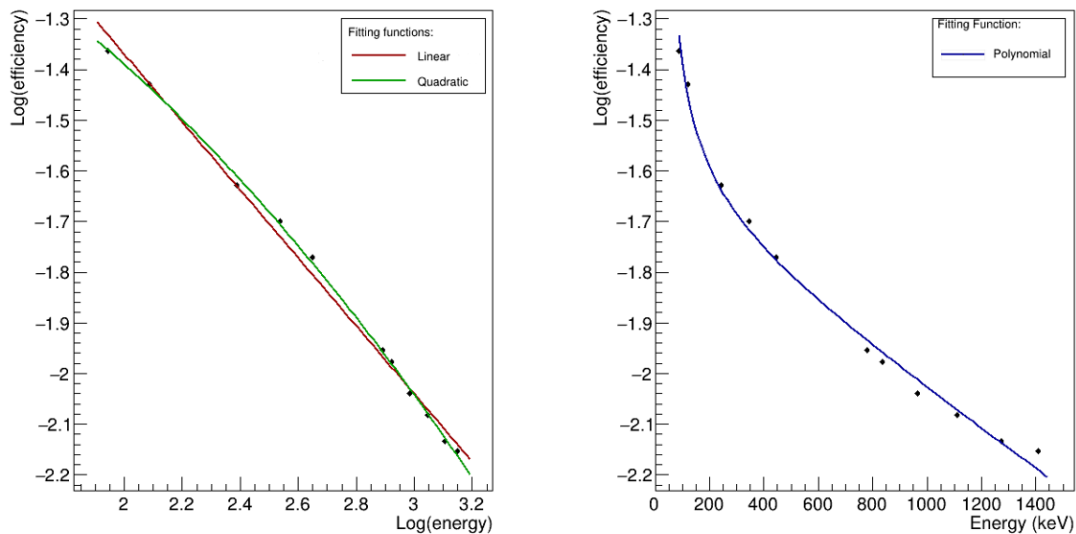


Figure 2.1.3.3: The procedure of fitting the efficiency using different fitting functions [18].

Three of the most commonly used fitting functions were used [14], more specifically:

- Linear: $\log(\varepsilon) = \alpha_0 + \alpha_1 \cdot \log(E)$
- Quadratic: $\log(\varepsilon) = \alpha_0 + \alpha_1 \cdot \log(E) + \alpha_2 \cdot (\log(E))^2$
- Polynomial: $\log(\varepsilon) = \alpha_0 \cdot E + \alpha_1 + \alpha_2 \frac{1}{E}$

As can be seen from the graph, the most suitable fitting function in this case is the quadratic.

2.2 Simulation

The final step to a full detector characterization is its modeling using simulations. In this work, this process was performed using the GEANT4 toolkit. The characterized detector can then be used to simulate different experimental conditions and calculate values which cannot be measured, such as the detector efficiency at different configurations and energies, or correction factors.

2.2.1 GEANT4

For the simulation of the detection system the GEANT4 toolkit was employed. GEANT4 (GEometry ANd Tracking) is implemented in the C++ programming language and is widely used for simulating the way particles pass through matter via the Monte Carlo method. It is used in many different fields, from nuclear and high energy physics, to astrophysics and biology. It utilizes a variety of physical models and experimental data in order to handle all physical processes (electromagnetic, hadronic, optical, etc.) that arise during the interaction of particles with matter.

First, the user defines the geometry of their physical problem using different volumes in order to create the simulation. Each volume is created through three basic concepts: the solid, the logical and the physical volume. A solid in GEANT4 is used to describe an object of specific shape and dimensions. The logical volume adds to the solid all its physical characteristics, such as its material. Finally, the physical volume includes its coordinates, rotation details etc. Each volume is placed inside a containing volume, referred to as “mother” volume and all the details of a “daughter” volume’s placement are relative to its “mother” volume. Consequently, if a “mother” volume is rotated or moved, all the “daughter” volumes will be rotated or moved accordingly. The largest volume that contains all other volumes is named “World” and is the first to be constructed.

Afterwards, the user has to attribute all the desired properties to the primary particles. In order to achieve this, the class `G4PrimaryGenerationAction` is employed. Using this class, the user can randomize and provide the initial values of a particle such as its type, position, energy, momentum, etc. Following the generation of the primary particle, GEANT4 tracks it until its kinetic energy drops below a certain limit, or until it goes out of the World volume, or it decays into different particles. In the latter case, GEANT4 also tracks the secondary particles. All information (kinetic energy, time, volume, type of particle, etc.) about the tracks and interactions caused by an initial particle is stored within an event. A set of events sharing the same set-up configuration, is referred to as a Run.

In order for GEANT to be able to accurately simulate the physical problem it must take into account physical models and experimental data. This is achieved via a variety of physics lists from which the user can choose the suitable one that contains the physical processes more relevant to their problem.

GEANT4 also offers the possibility for visualization of the simulation. The user can choose the elements of the simulation that they want to be depicted graphically (for example detector components, particle trajectories and hits, etc.) and attribute characteristics like colour. This can help the user to inspect the simulation and detect possible flaws [19].

2.2.2 Efficiency characterization

The simulation of the experimental setup has to be as precise as possible in order to achieve a correct characterization that can produce accurate results.

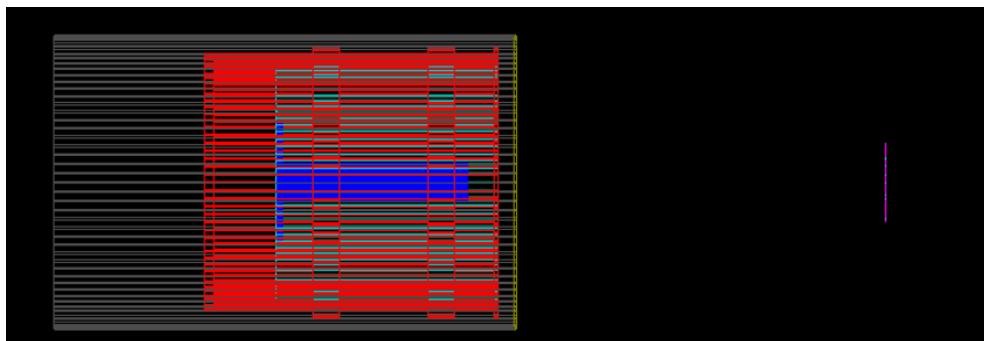


Figure 2.2.2.1: A GEANT visualization of the detector and the source. The purple color corresponds to the source, the carbon epoxy window to green, the outer aluminum to gray, the crystal holder to red, the crystal to light blue and the borehole and ring inside the crystal to blue.

The first step involves the creation of the simulation using the detector's specifications sheet. The results are compared to the experimental ones and the values of the detector characteristics are tuned in order to achieve maximal agreement between the experimental points and the simulation. An example of the comparison between the experimental data and the simulation according to the manufacturer is shown in Figure 2.2.2.2.

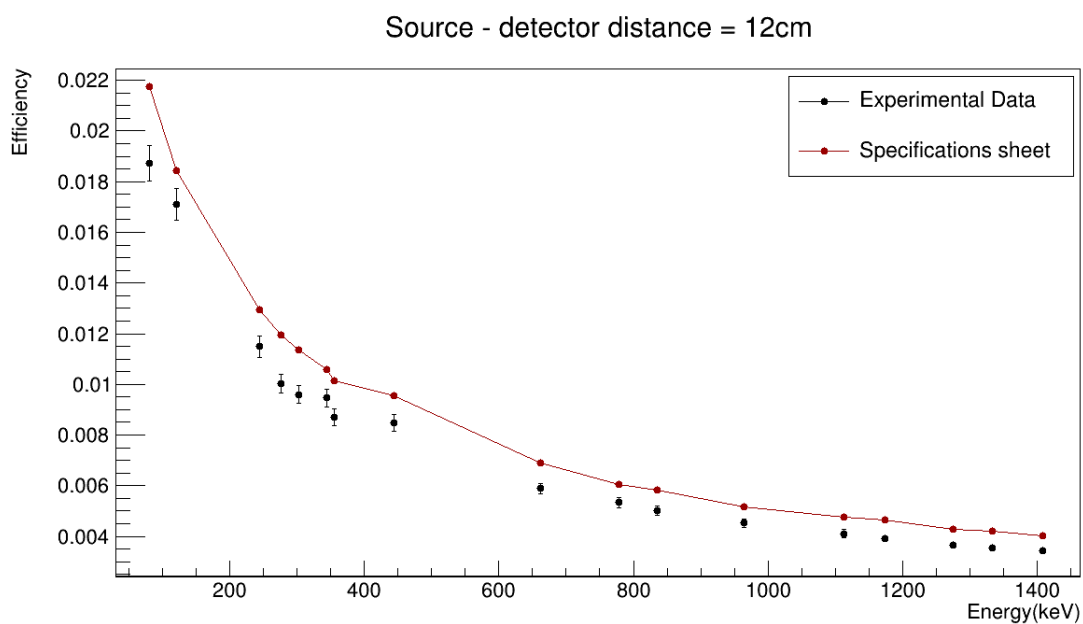


Figure 2.2.2.2: Comparison between experimental data (black) and a GEANT4 simulation according to the manufacturer's specifications sheet (red).

The deviations between the experimental values and the results from the GEANT4 simulation approached 20%, leading to the assumption that modifications to the detector geometry parameters would be necessary.

A systematic error appears in the simulations, which indicates that the window-to-crystal distance (gap) needs to be changed, since it affects all the measurements. Tuning only this parameter was not enough to reduce the deviation of the simulation from the experiment to an acceptable degree. The next steps, involve tests for different values in the geometry of the crystal. During this process, one keeps in mind that the length of the Ge crystal mainly affects high-energy γ -rays, as it provides “more material” to interact with, while the diameter of the crystal affects the solid angle.

After tuning the geometrical parameters of the detector, an adequate agreement of the simulation with the experimental data was achieved, as shown in Figure 2.2.2.3.

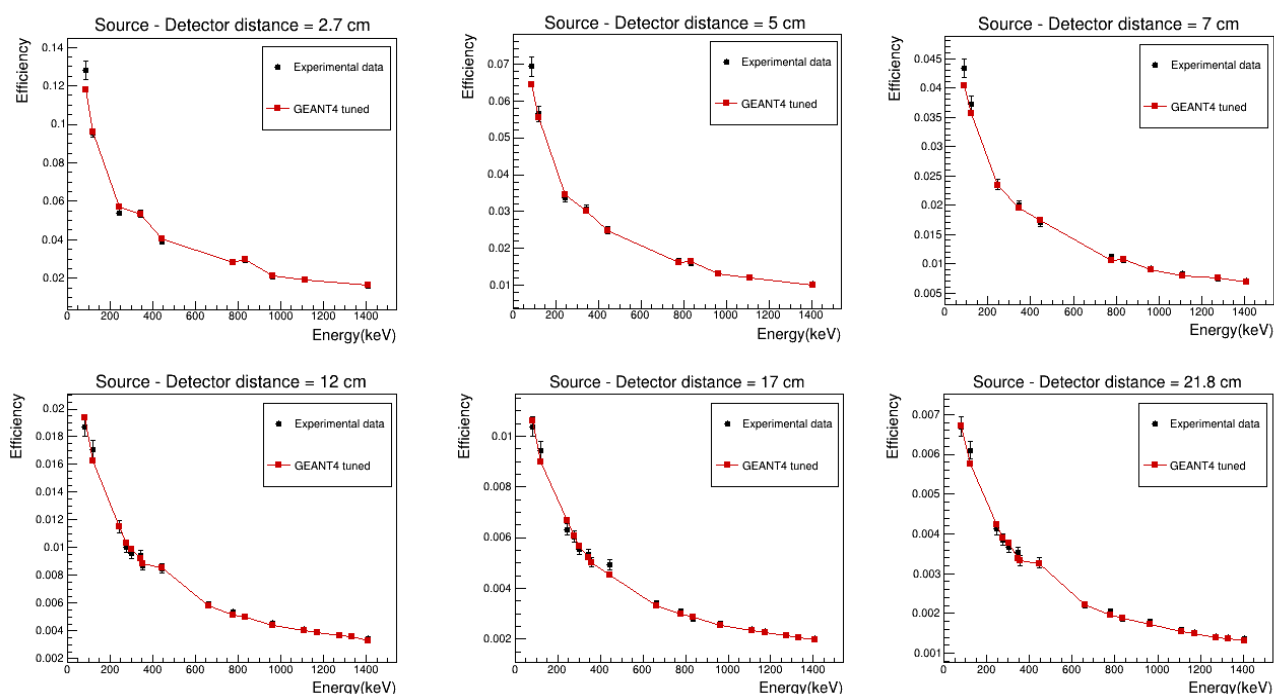


Figure 2.2.2.3: The experimental data (black) and the tuned GEANT4 (red) for one of the three detectors.

After the tuning process most of the simulation points lie within the experimental errors. The deviation between the experimental efficiency and the simulation is depicted in Figure 2.2.2.4.

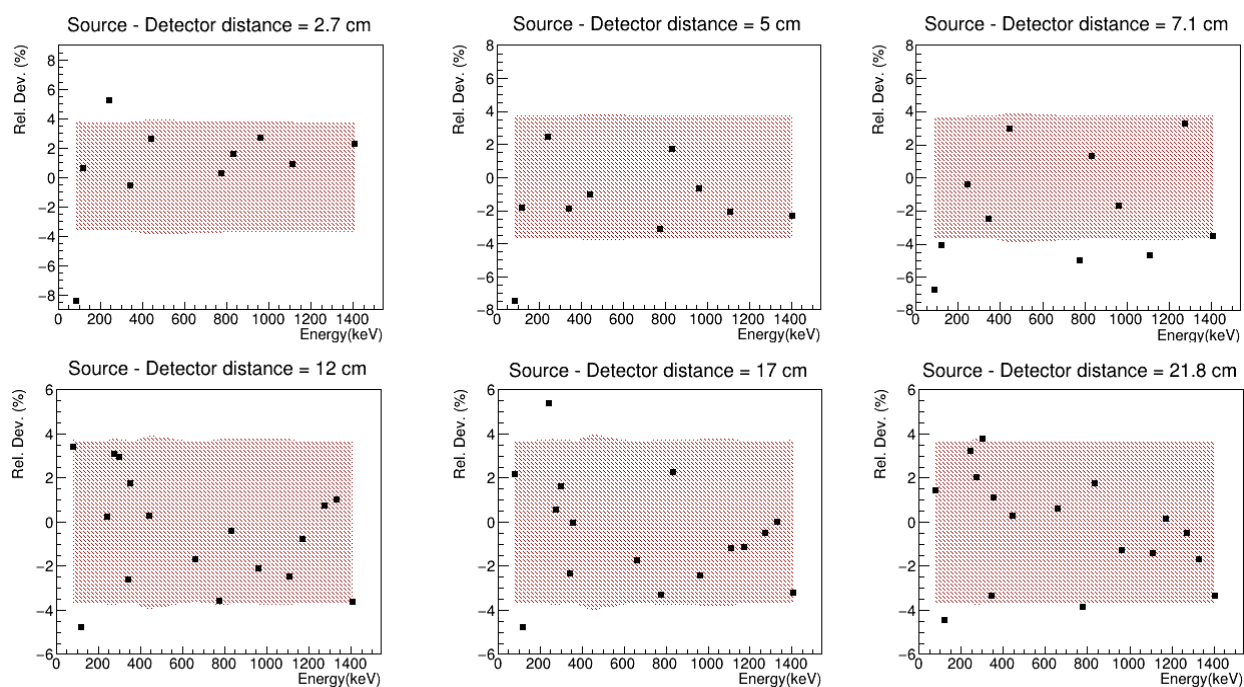


Figure 2.2.2.4: The black points correspond to the simulated full energy peak efficiency and the red band to the experimental uncertainty.

The majority of the simulated efficiency values lie within the measurement's uncertainty. Table 2.2.2.1 presents the tuned parameters together with the values of the specification's sheet.

	<u>Specification's sheet</u>	<u>GEANT4 tuned</u>
Gap (mm)	6	10.5
Crystal diameter (cm)	7.8	7.56
Crystal length (cm)	7.18	6.88

Table 2.2.2.1: The final GEANT4 tuned values for the simulation.

The same procedure was performed for the remaining two detectors. The results are presented below.

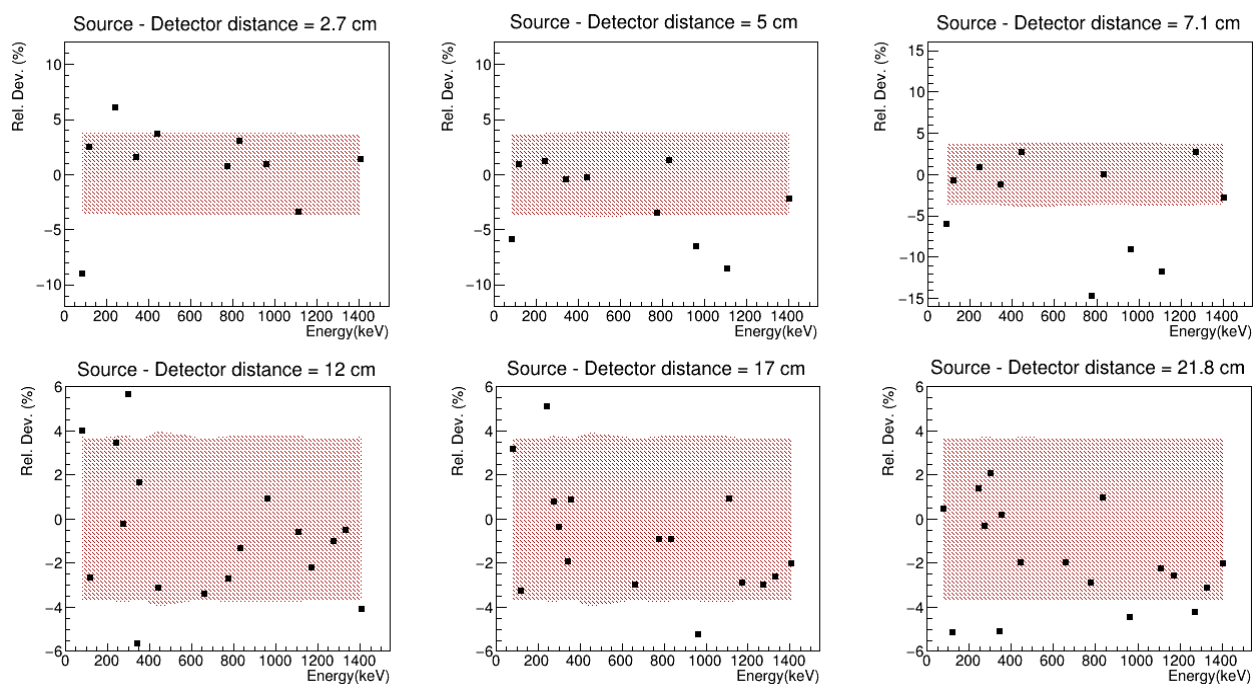


Figure 2.2.2.5: The deviation between the experimental efficiency and the simulation.

	Specification's sheet	GEANT4 tuned
Gap (mm)	6	10.1
Crystal diameter (cm)	7.5	7.3
Crystal length (cm)	7.49	7.34

Table 2.2.2.2: The final GEANT4 tuned values for the simulation.

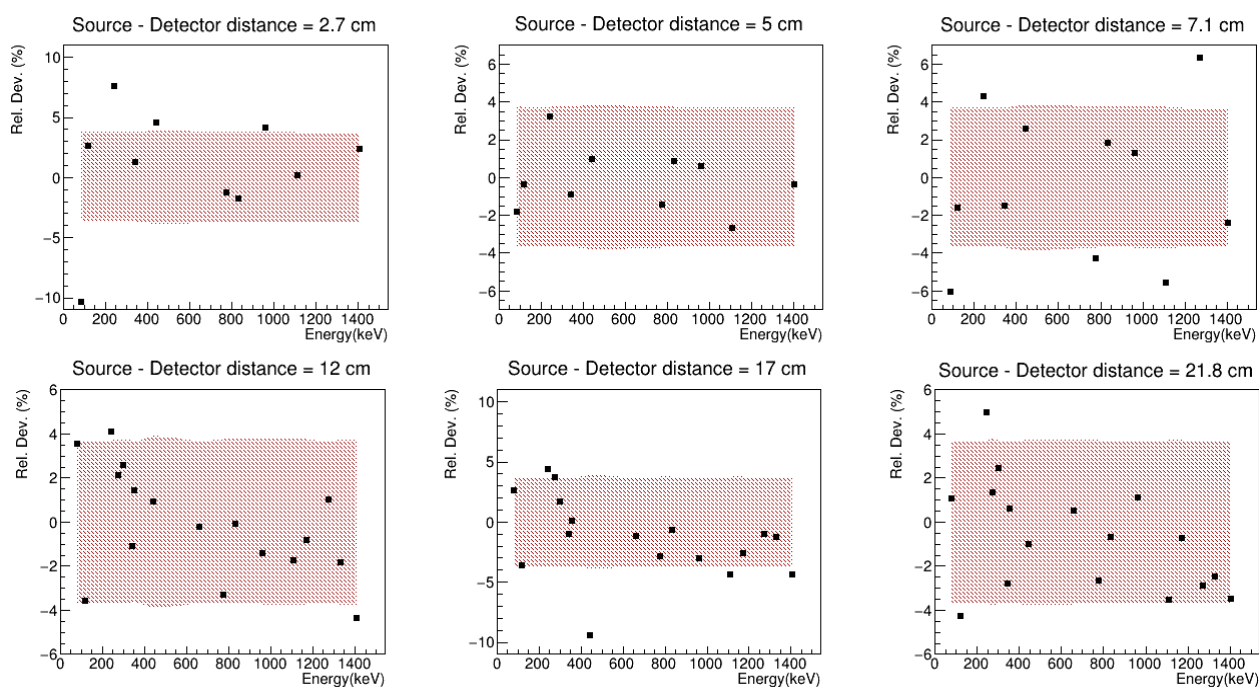


Figure 2.2.2.6: The deviation between the experimental efficiency and the simulation.

	<u>Specification's sheet</u>	<u>GEANT4 tuned</u>
<u>Gap (mm)</u>	6	9.5
<u>Crystal diameter (cm)</u>	7.49	7.25
<u>Crystal length (cm)</u>	7.45	7.3

Table 2.2.2.3: The final GEANT4 tuned values for the simulation.

Chapter 3 – Theoretical calculations

3.1 The TALYS code

TALYS is a code that simulates nuclear reactions in the energy range of 10^{-1} MeV – 10^3 MeV. It is a commonly used computer code that combines several macroscopic and microscopic models for the description and understanding of the nuclear reaction mechanisms and dynamics. Experimental data can be used so as to benchmark TALYS calculations and to improve the parameterization of the adopted models. Furthermore, it can be used for the generation of results where no experimental data are available.

The code simulates how a projectile hits a target nucleus by taking into account all the possible reaction channels. The necessary parameters that must be specified in the input file are the projectile type, the target and the energy of the projectile. In TALYS calculations, projectiles can be n, p, d, t, ^3H and α particles, whereas for a target, any nuclide with a mass number larger than 12 is available. Concerning the projectile energy, the user can choose either a single energy value or a range of different energies.

TALYS, as mentioned above, incorporates a number of different theoretical models that can be taken into account during the simulation. According to the projectile energy and the other user defined parameters as specified by the user the appropriate handling of theoretical models takes place in an integrated way. Figure 3.1.1 shows a schematic representation of the function and the incorporated models of the TALYS code.

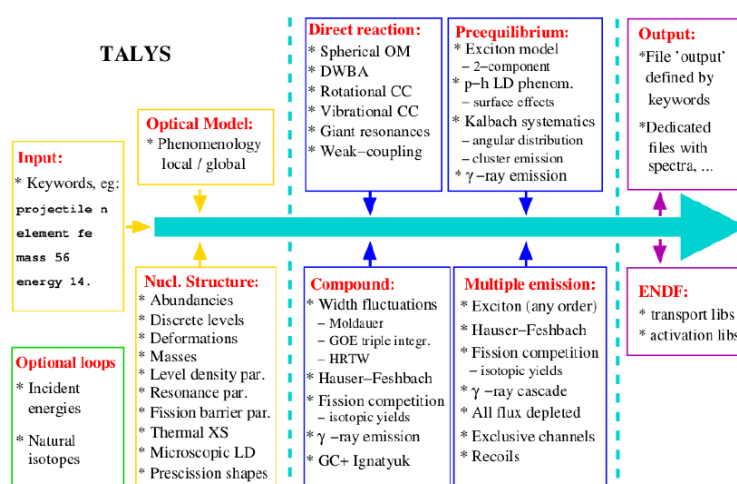


Figure 3.1.1: A simplified representation of the function of TALYS [12].

TALYS provides the user with a variety of calculations of physical quantities that different output files contain. Each file corresponds to an available channel of the reaction and a different type of calculation such as cross section, angular distribution or energy spectra etc. The user can choose the ejectile or residual nucleus characteristics according to the channel under study [12].

In the present study, the cross section of the three reactions was calculated through TALYS. During this process, the code takes into account all the possible reaction mechanisms that were described earlier (compound nucleus reactions, pre-equilibrium reactions, direct reactions) and the competition among the different reaction channels.

3.1.1 Cross section calculations for compound nucleus reactions

The predominant reaction mechanism in the case of the reactions that are under study in the present work, is the compound nucleus mechanism. The TALYS code performs the compound nucleus calculations using the Hauser-Feshbach theory, which is a quantum mechanical formalism that obeys in the conservation laws of energy, angular momentum and parity. According to this theory, the cross section for the reaction $A + \alpha \rightarrow C^* \rightarrow \alpha' + A'$ is given by the following formula:

$$\sigma_{\alpha\alpha'} = D^{comp} \frac{\pi}{\kappa^2} \sum_{J=mod(I+s,1)}^{l_{max}+I+s} \sum_{\Pi=-1}^1 \frac{2J+1}{(2I+1)(2s+1)} \times \sum_{j=|J-I|}^{J+I} \sum_{l=|j-s|}^{j+s} \sum_{j'=|J-I|}^{J+I} \sum_{l'=|j'-s'|}^{j'+s'} \delta_{\pi}(\alpha) \delta_{\pi}(\alpha') \frac{T_{alj}^J(E_a) \langle T_{a'l'j'}^J(E_{a'}) \rangle}{\sum_{a'',l'',j''} \delta_{\pi}(\alpha'') \langle T_{a''l''j''}^J(E_{a''}) \rangle} W_{alja'l'j'}^J$$

where:

E_a : energy of the projectile

s : spin of the projectile

π_0 : parity of the projectile

l : orbital angular momentum of the projectile

j : total angular momentum of the projectile

$$\delta_{\pi}(\alpha): \begin{cases} 1 & (-1)^l \pi_0 \Pi_0 = \Pi \\ 0 & \text{otherwise} \end{cases}$$

α : channel designation of the initial system of projectile and target nucleus:

$\alpha = \{a, s, E_a, E_x^0, I, \Pi_0\}$, where a is the projectile type and E_x^0 the excitation energy of the target nucleus (usually zero)

l_{max} : maximum l -value for projectile

S_a : separation energy of the projectile

$E_{a'}$: energy of the ejectile

s' : spin of the ejectile

π_f : parity of the ejectile

l' : orbital angular momentum of the ejectile

j' : total angular momentum of the ejectile

$$\delta_{\pi}(\alpha'): \begin{cases} 1 & (-1)^{l'} \pi_f \Pi_f = \Pi \\ 0 & \text{otherwise} \end{cases}$$

α' : channel designation of the final system of ejectile and residual nucleus:

$\alpha' = \{a', s', E_{a'}, E_x, I', \Pi_f\}$, where a' is the ejectile type, E_x the excitation energy of the residual nucleus

- I: spin of the target nucleus
 Π_0 : parity of the target
 I': spin of the residual nucleus
 Π_f : parity of the residual nucleus
 Π : parity of the compound system
 J: total angular momentum of the compound system
 k: wave number of the relative motion of the input channel
 T: transmission coefficient
 D_{comp} : depletion factor to account for direct and pre-equilibrium effects
 W: width fluctuation correction (WFC) factor, which takes into account the correlations between the input and output channel. It is due to this factor that the elastic channel becomes important at low incident energies, whereas it is negligible for energies above a few MeV [12].

3.1.2 Level Densities

Following the decay of the compound nucleus, the residual nucleus is left at an excitation energy E_x . In reality, there are several nuclear states with excitation energy E_x , which differ in the total spin J and in parity Π . The number of nuclear levels per MeV around an excitation energy E_x , for a certain spin J and parity Π is called level density and is denoted as $\rho(E_x, J, \Pi)$. There is a probability for the compound nucleus to decay in each of these states. The density of those levels increases rapidly as the excitation energy increases. Their spacing becomes smaller and their width constantly increases.

The level densities are taken into account in the calculation of the transmission coefficients in the Hauser-Feshbach theory through the integral:

$$\langle T_{a'l'j'}^J(E_{a'}) \rangle = \int_{E_x - \frac{1}{2}\Delta E_x}^{E_x + \frac{1}{2}\Delta E_x} \rho(E_{x'}, J, \Pi) dE_{x'} T_{a'l'j'}^J(E_{a'})$$

At low excitation energies the discrete states are known. Instead, at higher energies several theoretical level density models have been developed [12].

The TALYS code provides the user with six different options for describing the level densities. Three of them are phenomenological and three microscopic. The user can control which model will be used for the calculation by giving the appropriate keyword (ldmodel #) to the input file. The available options will be briefly presented below.

Constant Temperature and Fermi Gas model

The Fermi Gas model (FGM) is the best known analytical level density expression and is related to all the phenomenological models that will be discussed. Based on this model, the excited

levels of the nucleus, which are constructed by the single particle states, are equally spaced and collective levels are absent. The Fermi gas level density around an excitation energy E_x , for a certain spin J and parity Π , is given by

$$\rho_F(E_x, J, \Pi) = \frac{1}{2} \frac{2J+1}{2\sqrt{2\pi}\sigma^3} e^{-\frac{(J+\frac{1}{2})^2}{2\sigma^2}} \frac{\sqrt{\pi}}{12} \frac{e^{2\sqrt{a}U}}{a^{1/4}U^{5/4}}$$

where:

σ^2 : spin cut-off parameter, which represents the width of the angular momentum distribution and depends on the excitation energy

a : the level density parameter

U : effective excitation energy equal to $E_x - \Delta$ and

Δ : empirical parameter which is included to simulate odd-even effects in nuclei called pairing energy.

The level density can be written in the simpler form

$$\rho_F(E_x, J, \Pi) = \frac{1}{2} R_F(E_x, J) \rho_F^{tot}(E_x)$$

where:

the Fermi gas spin distribution is: $R_F(E_x, J) = \frac{2J+1}{2\sigma^2} e^{-\frac{(J+\frac{1}{2})^2}{2\sigma^2}}$ and

the total Fermi gas level density summed over all spins and parities:

$$\rho_F^{tot}(E_x) = \frac{1}{\sqrt{2\pi}\sigma} \frac{\sqrt{\pi}}{12} \frac{e^{2\sqrt{a}U}}{a^{1/4}U^{5/4}}$$

In the Constant Temperature Model (CTM) (keyword: ldmodel 1), the excitation energy range is divided into two parts. For the low energy part the so-called constant temperature law applies and for the high energy part the Fermi gas model applies. Specifically, for the level density we have:

$$\rho(E_x, J, \Pi) = \begin{cases} \frac{1}{2} R_F(E_x, J) \rho_{CTM}^{tot}(E_x) & \text{if } E_x \leq E_M \\ \rho_F(E_x, J, \Pi) & \text{if } E_x \geq E_M \end{cases}$$

where:

E_M : the matching energy where the two formulas must be in agreement.

R_F : the Fermi gas spin distribution

and $\rho_{CTM}^{tot}(E_x) = \frac{1}{T} e^{\frac{E_x - E_0}{T}}$ [12].

The Back-shifted Fermi Gas model

The second model is called Back-shifted Fermi gas model (keyword: ldmodel 2). In this case, the Fermi gas expression is used throughout the whole energy range. One problem that occurs is that the level density becomes infinite at zero excitation energy. This was solved by Demetriou and Goriely using the theory of Grossjean and Feldmeier. In this case the level density is calculated using the formula:

$$\rho_{BFM}^{tot}(E_x) = \left[\frac{1}{\rho_F^{tot}(E_x)} + \frac{1}{\rho_0(t)} \right]^{-1}$$

where:

$$\rho_0(t) = \frac{e}{24\sigma} \frac{(a_n + a_p)^2}{\sqrt{a_n a_p}} e^{4a_n a_p t^2}, \quad a_n = a_p = \frac{a}{2}$$

and t is called thermodynamic temperature and is given by $t = \sqrt{\frac{U}{a}}$.

Using the usual spin distribution the level density is given by:

$$\rho_{BFM}(E_x, J, \Pi) = \frac{1}{2} \frac{2J+1}{2\sigma^2} e^{-\frac{(J+\frac{1}{2})^2}{2\sigma^2}} \rho_{BFM}^{tot}(E_x) \quad [12].$$

The generalized superfluid model

The Generalized Superfluid Model (GSM) (keyword: ldmodel 3) also distinguishes between a low energy and a high energy region like the Constant Temperature Model does, but in this case this distinction does not depend on specific discrete levels that determine a matching energy, instead it follows naturally from the theory. At low excitation energies a superfluid behaviour appears, where pairing correlations strongly influence the level density. At high energies the Fermi gas model applies.

$$\rho(E_x, J, \Pi) = \begin{cases} \frac{1}{2} R_F(E_x, J) \rho_{GSM}^{tot}(E_x) & U' \leq U_C \\ \frac{1}{2} R_F(E_x, J) \rho_F^{tot}(E_x) & U' \geq U_C \end{cases}$$

where:

U': effective excitation energy

U_C: critical energy defined based on thermodynamical functions

$$\rho_{GSM}^{tot} = \frac{1}{\sqrt{2\pi\sigma}} \frac{e^S}{\sqrt{D}}$$

where:

S: the entropy of the nucleus

D: determinant

In the equations above, the entropy, the determinant and the spin cutoff parameter are defined in terms of U_C and U' [12].

Microscopic models

Besides the phenomenological models that are used in TALYS, there is also an option to employ microscopic approaches to describe the nucleus. The three microscopic level density models are:

1. microscopic level density model 1: S. Goriely et al. (keyword: ldmodel 4)
2. microscopic level density model 2: S. Goriely et al. (keyword: ldmodel 5)
3. microscopic level density model 3: S. Hilaire et al. (keyword: ldmodel 6)

3.2 TALYS calculations for the excitation functions

A comparison is made between the excitation function calculated for each available TALYS level density model and the existing experimental data.

3.2.1 Excitation function of the reaction $^{127}\text{I}(n,2n)^{126}\text{I}$

Figure 3.2.1.1 shows the excitation function for the case of the reaction $^{127}\text{I}(n,2n)^{126}\text{I}$. The colored lines show the excitation function calculated by TALYS using different models for the level densities, the dotted line shows the ENDF data [21], while in the same graph the previous experimental measurements are presented [9].

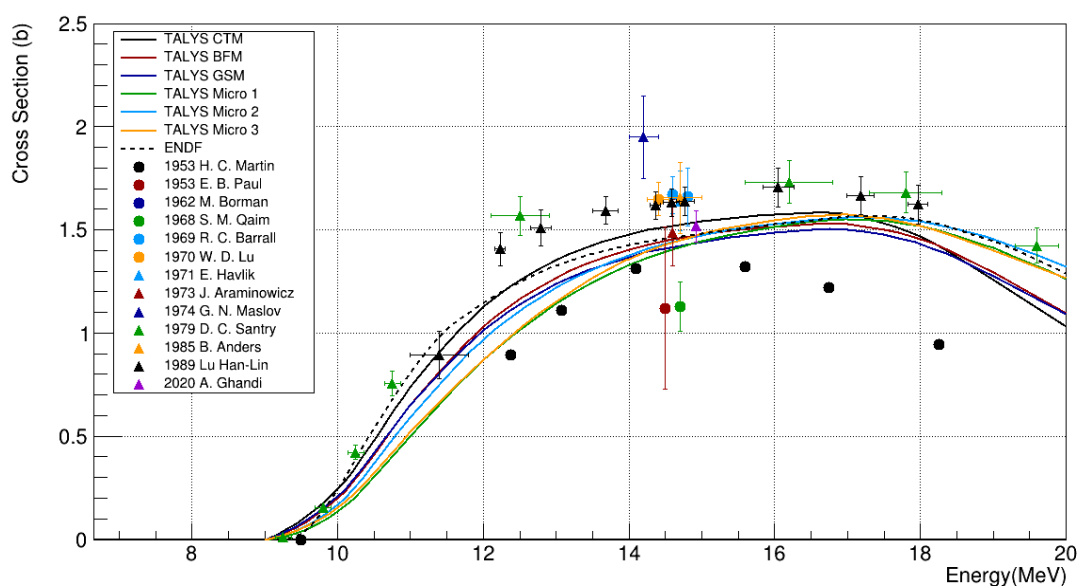


Figure 3.2.1.1: The comparison between the TALYS results and the existing experimental data in the case of $^{127}\text{I}(n,2n)^{126}\text{I}$.

The six theoretical models give different results across the entire energy range. The Back-shifted Fermi Gas model approaches the Generalized Superfluid Model, while the Constant Temperature and Fermi Gas Model deviate considerably. Meanwhile, the microscopic models show common behaviors at the high energy region. A noticeable fact is that none of the models appear to be able to adequately approach the experimental data. In particular, the entirety of the most recent measurements, that at the same time cover a broad energy range, leads to higher values for the cross section than any of the theoretical results.

3.2.2 Excitation function of the reaction $^{133}\text{Cs}(n,2n)^{132}\text{Cs}$

Figure 3.2.2.1 shows the excitation function for the reaction $^{133}\text{Cs}(n,2n)^{132}\text{Cs}$.

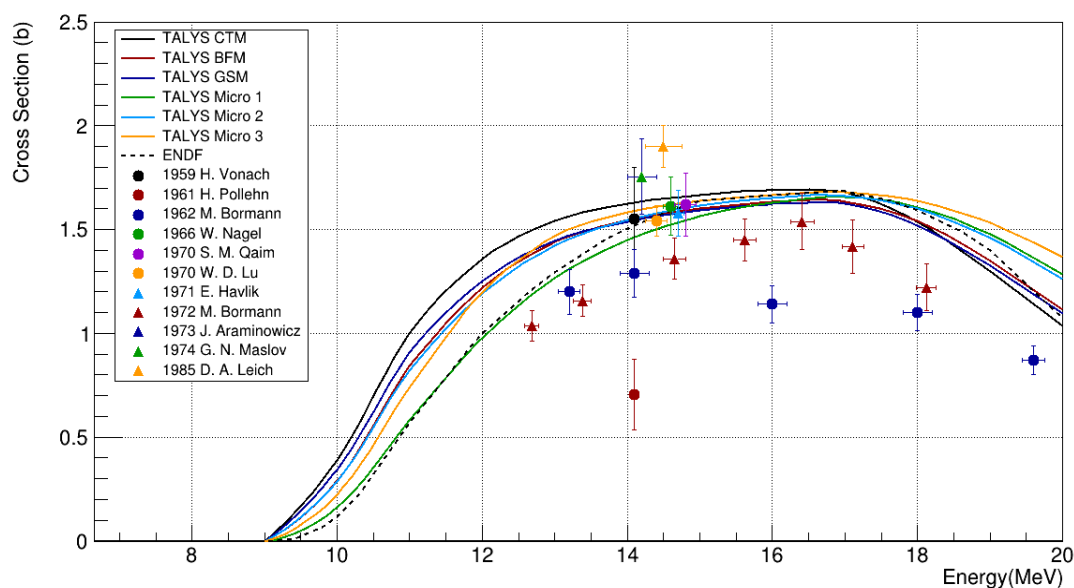


Figure 3.2.2.1: The comparison between the TALYS results and the existing experimental data in the case of $^{133}\text{Cs}(n,2n)^{132}\text{Cs}$.

Strong discrepancies once again appear between the models and the experimental data. The deviation between the models is particularly pronounced in the low energy part, up to the energy of 15 MeV. The same behavior is observed at energies higher than 17 MeV, where the microscopic models give higher values of cross section than the rest models. As observed in the previous case, there is a discrepancy between the theoretical calculations and the experimental data, as a variety of experimental results lead to smaller values of cross section than the theoretical models.

3.2.3 Excitation function of the reaction $^{136}\text{Ce}(n,2n)^{135}\text{Ce}$

Figure 3.2.3.1 shows the excitation function for the reaction $^{136}\text{Ce}(n,2n)^{135}\text{Ce}$.

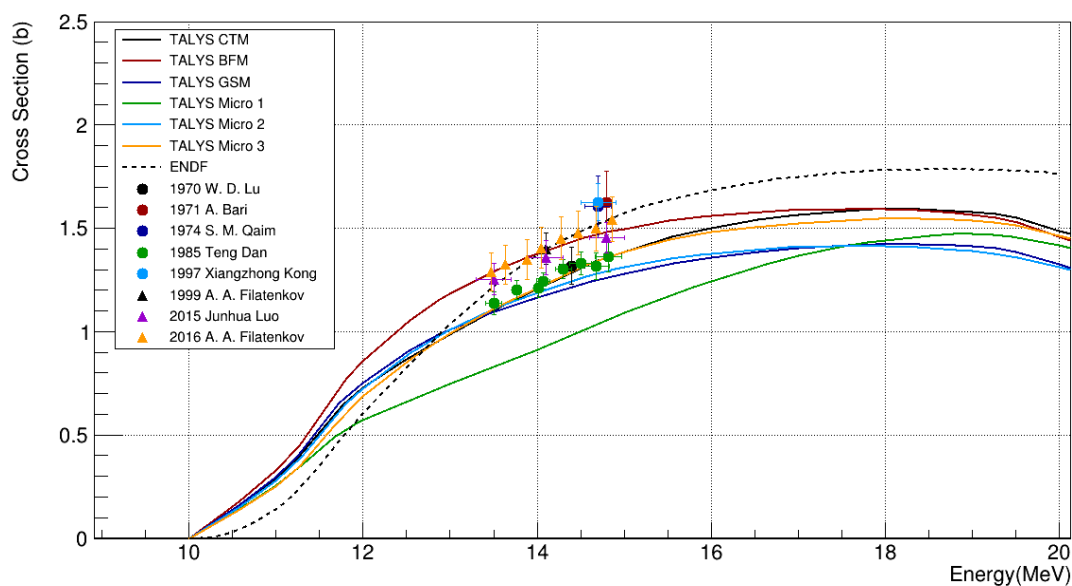


Figure 3.2.3.1: The comparison between the TALYS results and the existing experimental data in the case of $^{136}\text{Ce}(n,2n)^{135}\text{Ce}$.

In the case of this reaction, the most pronounced differences between the models are observed. The discrepancies are strong throughout the whole energy range, except at the low energy part where the models seem to approach each other. However, the available experimental data for the reaction are minimal and the entirety of them lie between 13 and 15 MeV. There are no experimental data available either at the lower or at the higher energy part, which makes any comparison with the theoretical calculations incomplete.

Due to the pronounced discrepancies between the different theoretical models and the lack of experimental data over a larger energy range, no conclusion can be drawn as to which model is more suitable to be used for the calculations of the cross section of the reactions under study. For this reason, the cross section used in the continuation of this work and the calculation of the expected counting rates, will be extracted directly from the ENDF library [21], in order to provide a better estimation of the expected statistics.

A general conclusion that can be drawn is that for the three physics cases large discrepancies can be observed between the existing experimental data. Also the experimental information for the $^{133}\text{Cs}(n,2n)^{132}\text{Cs}$ and $^{136}\text{Ce}(n,2n)^{135}\text{Ce}$ reactions is completely missing for extended energy regions. At the same time, by adopting different level density models strong deviations can be observed in the theoretical estimates of the excitation functions.

For all these reasons, the feasibility study through the present work and eventually the experimental and theoretical study of the aforementioned (n,2n) reaction is important for fundamental research purposes.

◆ Chapter 4 – Expected counting rates ◆

The final scope of this study was to calculate the expected counting rates of the reactions $^{127}\text{I}(n,2n)^{126}\text{I}$, $^{133}\text{Cs}(n,2n)^{132}\text{Cs}$ and $^{136}\text{Ce}(n,2n)^{135}\text{Ce}$. The detectors' efficiency was obtained by GEANT4 simulations and the cross section values were taken from the ENDF library [21].

4.1 Tandem Accelerator Facility

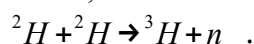
The Institute of Nuclear and Particle Physics hosts an electrostatic Van de Graaff Tandem accelerator with a maximum acceleration voltage of 5.5 MV. It is a low-energy ion-beam facility, one of the few accelerators of its kind in Europe, which started operating in the 1973 [1].



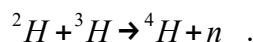
Figure 4.1.1: The Tandem laboratory at INPP of Demokritos (left) and the Van de Graaff generator (right) [1].

Neutron beams are always secondary beams produced by nuclear reactions. Depending on the reaction that generates the neutrons, the main beam characteristics, the neutron beam energy and the specific experimental conditions change. The neutron beams required for the study of the three aforementioned reactions at the energies mentioned earlier, will be produced by the Demokritos accelerator via two reactions, the D-D reaction and the D-T reaction.

The D-D is an exothermic reaction with a Q value equal to 3.27 MeV. During this reaction, a deuteron nucleus interacts with another deuteron nucleus producing a tritium nucleus and a neutron, which is written as



The D-T reaction is an exothermic reaction as well, with a corresponding Q value equal to 17.59 MeV. In this case a deuteron nucleus interacts with a tritium nucleus, producing a helium nucleus and a neutron, which is



The neutron beams between 10-11 MeV will be produced using the D-D reaction, whereas for the higher energies between 17-20 MeV, the D-T reaction will be utilized on account of its higher Q value.

4.2 Energy diagrams of the reactions

After bombarding the three isotopes ${}^{127}\text{I}$, ${}^{133}\text{Cs}$ and ${}^{136}\text{Ce}$ with the neutron beam, the compound nuclei ${}^{128}\text{I}^*$, ${}^{134}\text{Cs}^*$ and ${}^{137}\text{Ce}^*$ will be produced accordingly.

In general, assuming the reaction $a + A \rightarrow C^* \rightarrow a' + A'$, the excitation energy of the compound nucleus is given by

$$E_{ex} = S_n + E_{n, CMS}$$

where:

S_n : neutron binding energy in the compound nucleus

$E_{n, CMS}$: the neutron beam energy at the Center of Mass System

The neutron binding energy is given from the equation

$$S_n = \Delta(A) + \Delta(\alpha) - \Delta(C^*)$$

where:

Δ : represents the mass excess of the corresponding nuclei

The neutron beam energy at the center of mass system is dependent on the laboratory neutron beam energy via the equation

$$E_{n, CMS} = E_{n, Lab} \frac{A_A}{A_{C^*}}$$

where:

$E_{n, Lab}$: the laboratory neutron beam energy

A: mass number of the corresponding nuclei

The excited compound nucleus can then decay in a variety of different ways. The decay probability depends only on the energy given to the system and not the input channel, as suggested by the Bohr Independence theory mentioned before. According to the above information regarding the excitation energy of the compound nucleus and the required energy for each reaction channel, the energy diagrams for the three reactions are presented below.

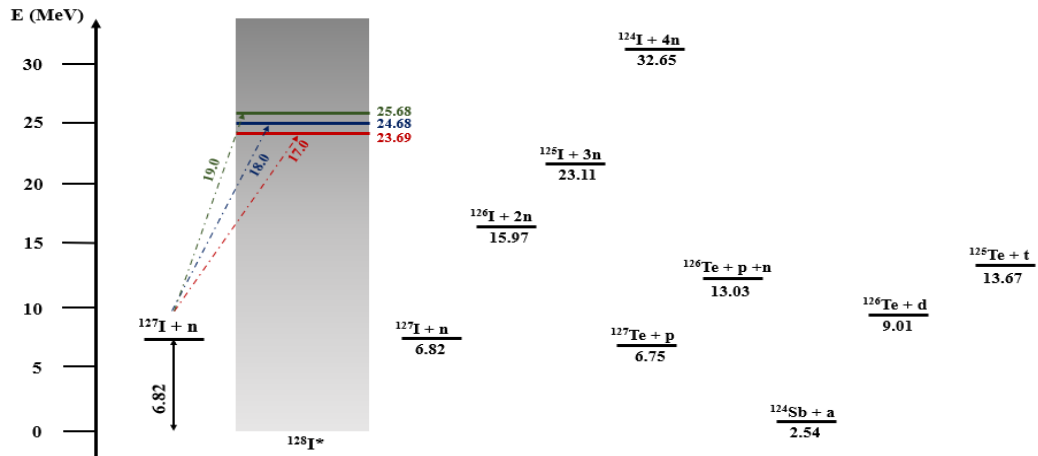


Figure 4.2.1: The energy diagram for the $^{127}\text{I} + n$ reaction.

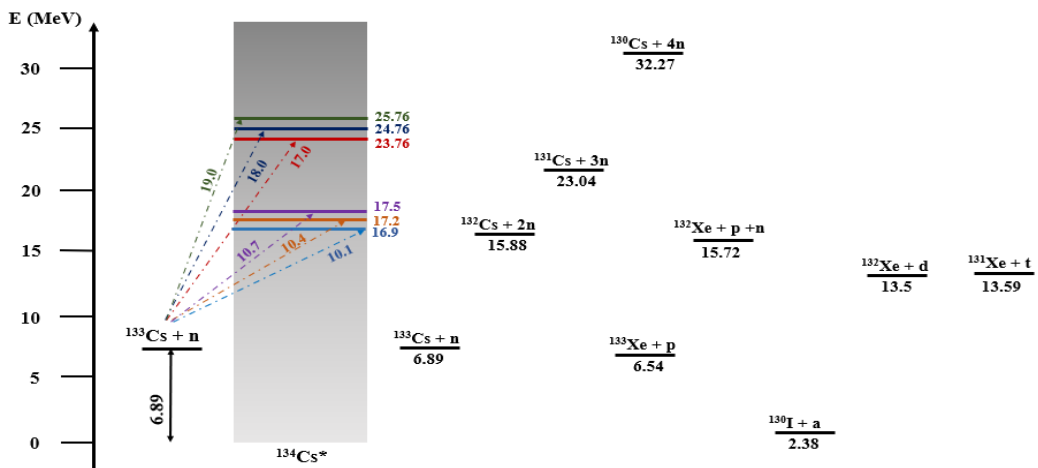


Figure 4.2.2: The energy diagram for the $^{133}\text{Cs} + n$ reaction.

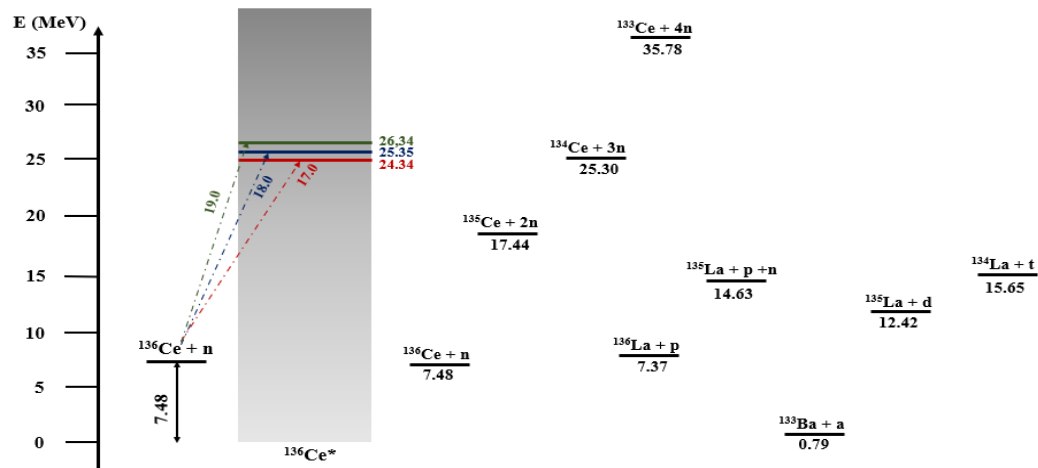


Figure 4.2.3: The energy diagram for the $^{136}\text{Ce} + n$ reaction.

The energy levels of the output channel are calculated using the following equation

$E_{out} = \Delta(C^*) - \Delta(a') - \Delta(A')$. All the channels that lie below the excitation energy of the compound nucleus, will be available as output channels and must be studied further.

4.3 Expected counting rates

According to the activation technique the expected counting rate can be calculated via the equation

$$counts = \sigma \cdot \Phi \cdot N_T \cdot \varepsilon \cdot I_\gamma \cdot e^{-\lambda t_w} \cdot (1 - e^{-\lambda t_m}) \cdot f_B$$

where:

σ : the reaction cross section

Φ : total beam flux

N_T : number of target nuclei in the sample

ε : efficiency of the detector at the energy of the emitted radiation for the geometry of the measurement

I_γ : intensity of the emitted radiation

λ : decay constant of the daughter nucleus

t_w : waiting time between the end of the irradiation and the start of the measurement

t_m : measurement time

f_B : the correction factor for the product nuclei decay during irradiation

Assuming that the flux of the beam is constant the f_B factor is given by

$$f_B = \frac{1 - e^{-\lambda t_{irr}}}{\lambda} t_{irr}$$

where:

t_{irr} : irradiation time

The number of target nuclei that the sample contains is equal to

$$N_T = \alpha v \frac{m N_A}{MW}$$

where:

α : abundance of the mother nucleus in the natural composition

v : number of atoms of the nucleus under study in the target material

m : mass of the sample

N_A : Avogadro number

MW : molecular weight of the nuclei contained into the sample

The expected neutron flux at the INPP facilities was estimated considering previous measurements [6-8]. Furthermore, GEANT4 simulations were performed in order to calculate the detector's efficiency at the energy of the emitted radiation for each physics case.

4.3.1 Expected counting rate of the reaction $^{127}\text{I}(n,2n)^{126}\text{I}$

The isotope of ^{126}I has a lifetime of 12.93 days and decays either to ^{126}Te via 52.7% ϵ (EC + β^+) or to ^{126}Xe via 47.3% β^- decay emitting several γ and x-rays [22]. The γ -ray used within this work is the strongest one. The decay properties of the product nuclei, which are used for the calculations of the expected counting rate, are presented in Table 4.3.1.1 below.

Half life	Energy of γ-ray (keV)	I_γ (%)
(12.93 \pm 0.05) d	388.6	35.6

Table 4.3.1.1: The decay properties of the ^{126}I [22].

For this purpose, KI samples with a mass of 0.5 g are proposed. The ^{127}I isotope is 100% abundant [22]. In order to obtain satisfying counting rate different measurement, waiting and irradiation times were studied, for specific measuring geometries. The results are summarized in Table 4.3.1.2.

Neutron energy (MeV)	Detector distance (cm)	Irradiation Time (hours)	Waiting Time (min)	Measuring Time (hours)	Counts at 388.6 keV photopeak
17	5	3	50	7	10600
18	5	5	50	8	10500
19	5	5	50	7	10500

Table 4.3.1.2: The expected counting rate for the reaction $^{127}\text{I}(n,2n)^{126}\text{I}$. The cross section used in the calculations was extracted from the ENDF library [21].

As can be seen in Table 4.3.1.2 excellent statistical uncertainty is expected for the given detection geometry and counting conditions.

For a complete feasibility study, an examination of the possible contamination of the peak must be performed. This can occur when unstable isotopes are produced through other "open" reactions channels on the same or other isotopes present in the sample material. In this case it can happen, one or more of the emitted γ -rays to be very close in energy with the γ -rays of interest. Thankfully, considering the irradiation conditions and the sample composition, no interference effects are expected for the 388.6 keV γ -ray.

Another possible source of contamination of the γ -ray is the background radiation of the experimental area. For this reason a background spectrum was obtained at the Tandem accelerator facility at Demokritos, using one of the three detectors that were characterized in this study, as mentioned before. The analysis of the background spectrum shows no possible sources of contamination for the γ -ray under study.

4.3.2 Expected counting rate of the reaction $^{133}\text{Cs}(n,2n)^{132}\text{Cs}$

The isotope of ^{132}Cs has a lifetime of 6.48 days and decays either to ^{132}Xe via 98.13% ϵ (EC + β^+), or to ^{132}Ba via 1.87% β^- decay emitting several γ and x-rays [22]. As in the previous case, the γ -ray used within this work is the stronger one. The decay properties of the product nuclei, which are used for the calculations of the expected counting rate, are presented in Table 4.3.2.1 below.

<u>Half life</u>	<u>Energy of γ-ray (keV)</u>	<u>I_γ (%)</u>
(6.480 \pm 0.006) d	667.7	97.59

Table 4.3.2.1: The decay properties of the ^{132}Cs [22].

For this purpose, CsCl samples with a mass of 0.5 g are considered. The ^{133}Cs isotope is 100% abundant [22]. The results are summarized in Table 4.3.2.2.

<u>Neutron energy (MeV)</u>	<u>Detector distance (cm)</u>	<u>Irradiation Time (hours)</u>	<u>Waiting Time (min)</u>	<u>Measuring Time (hours)</u>	<u>Counts at 667.7 keV photopeak</u>
10.1	5	10	50	20	4300
10.4	5	10	50	20	7500
10.7	5	8	50	20	10700
17	5	2	50	3	11200
18	5	2	50	6	11100
19	5	2	50	5	10000

Table 4.3.2.2: The expected counting rate for the reaction $^{133}\text{Cs}(n,2n)^{132}\text{Cs}$. The cross section used in the calculations was extracted from the ENDF library [21].

In this case, the (n,a) and (n,d) reactions could influence the observable spectrum. The information about the γ -rays resulting from those reactions and the corresponding counting rate are presented in the Table 4.3.2.3.

$^{133}\text{Cs}(n,a)^{130}\text{I}$ with γ -ray energy: 668.5 keV	
<u>Neutron energy (MeV)</u>	<u>Counts</u>
10.1	40
10.4	45
10.7	55

17	170
18	180
19	200
$^{133}\text{Cs}(\text{n,d})^{132}\text{Xe}$ with γ-ray energy: 667.7 keV	
<u>Neutron energy (MeV)</u>	<u>Counts</u>
10.1	0
10.4	0
10.7	0
17	0
18	0
19	0

Table 4.3.2.3: The possible contamination from the other open channels and the corresponding counting rate. The cross section used in the calculations was extracted from the ENDF library [21].

The (n,d) channel provides zero counts due to the very small lifetime of the ^{132}Xe isotope (8.39 ms) [22]. On the contrary, the (n,a) channel can compromise the results of the γ -ray under study, however, the expected correction factor in the recorded photopeak counts and the induced systematic uncertainty in the data will be minimal.

Furthermore, background contamination of the γ -ray under study is possible, as can be seen in Figure 4.3.2.1. For this reason, the background radiation must be subtracted from the measured spectrum before the analysis.

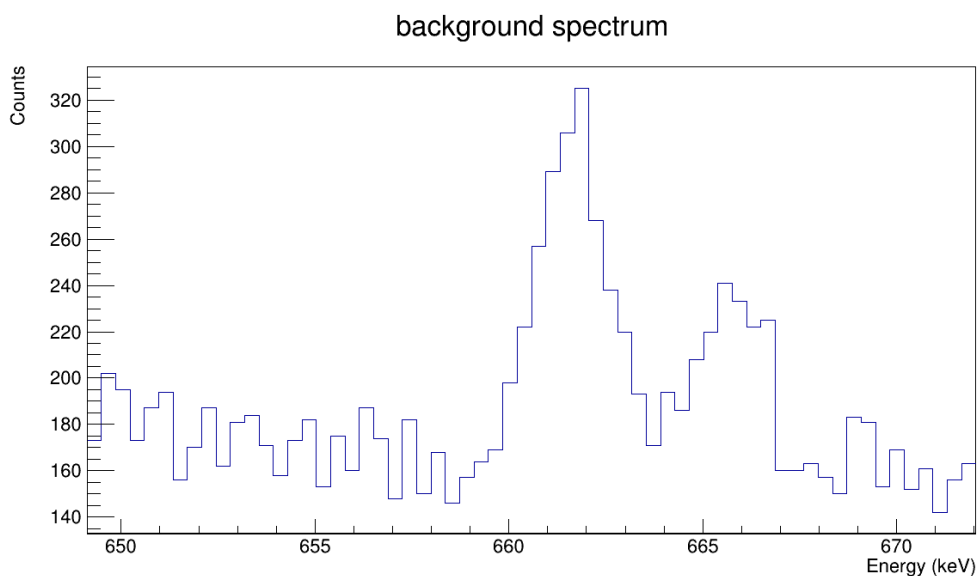


Figure 4.3.2.1: Background contamination for the 667.7 keV photopeak.

4.3.3 Expected counting rate of the reaction $^{136}\text{Ce}(n,2n)^{135}\text{Ce}$

The isotope of ^{135}Ce has a lifetime of 17.7 hours and decays to ^{135}La via 100% ϵ (EC + β^+) [22]. The decay properties of the product nuclei are presented in Table 4.3.3.1.

<u>Half life</u>	<u>Energy of γ-ray (keV)</u>	<u>I_γ (%)</u>
(17.7 \pm 0.3) h	265.6	41.8

Table 4.3.3.1: The decay properties of the ^{135}Ce [22].

For this purpose, CeO_2 samples with a mass of 1 g were proposed. The Ce element has many stable isotopes with ^{136}Ce isotope being the one with the minor abundance (0.185%) [22], which makes it difficult to collect enough counts in a short period of time. The results of the calculations of the expected statistics are summarized in Table 4.3.3.2.

<u>Neutron energy (MeV)</u>	<u>Detector distance (cm)</u>	<u>Irradiation Time (hours)</u>	<u>Waiting Time (min)</u>	<u>Measuring Time (hours)</u>	<u>Counts at 265.6 keV photopeak</u>
17	5	8	50	24	5100
18	5	10	50	24	3300
19	5	10	50	24	4000

Table 4.3.3.2: The expected counting rate for the reaction $^{136}\text{Ce}(n,2n)^{135}\text{Ce}$. The cross section used in the calculations was extracted from the ENDF library [21].

In order to increase the counting rate, a second detector can be used. The detector will be placed directly across the first one, in order to increase the solid angle and double the counts. Another way to achieve this, is by moving the detector even closer to the sample. This, however, can lead to summing effects that need to be taken into account and be corrected during the data analysis. Furthermore, no contamination of the recorded photopeak counts is expected in this reaction study.

Chapter 5 – Conclusions

The scope of this work was to investigate whether it is possible for three neutron induced reactions to be performed at the facilities of the Institute of Nuclear and Particle Physics at the National Centre of Science Research “Demokritos”, using the activation technique.

Three coaxial n-type HPGe detectors were characterized in terms of their efficiency using ^{152}Eu , ^{60}Co , ^{137}Cs , ^{133}Ba , ^{54}Mn , ^{22}Na and ^{109}Cd calibration sources measured in six source-to-detector distances from 2.7 to 21.8 cm. The characterization was then used to calculate the efficiency of the detector for the γ -rays with the biggest intensities emitted from the neutron induced reactions $^{127}\text{I}(n,2n)^{126}\text{I}$, $^{133}\text{Cs}(n,2n)^{132}\text{Cs}$ and $^{136}\text{Ce}(n,2n)^{135}\text{Ce}$.

The cross section of the three reactions was studied using the TALYS code. The study was focused on the available level densities models included in the package. The large discrepancies among the existing experimental data, as well as, the strong dependence of the theoretical calculations for different level density models, strongly suggest that further experimental investigation is needed, so as to provide firm constraints on the theoretical calculations and improve our understanding with respect to the reaction mechanisms.

The calculation of the counting rates was performed using the formula for the activation technique. In order to acquire adequate statistics for the measurements an estimation of the irradiation and measurement times was made. The two reactions that concern 100% abundant isotopes (^{127}I and ^{133}Cs), provide a large number of events for short irradiation times. In the case of the ^{136}Ce isotope, the expected counting rate is very low due to its very low abundance. In order to obtain adequate statistics, it is necessary to irradiate the samples longer and measure them for considerably longer times. Another way to fix this problem, is by implementing a second detector in order to increase the solid angle, thus the counting rate, or by moving the samples closer to the detectors and correct for the summing effects later on.

Furthermore, all possible interference reactions, as well as, possible contamination of the γ -ray energy due to reactions that lead to the emission of γ -rays close to the ones under study or interference of the background spectrum, were investigated. In most cases the γ -rays under study seem to be “pure”, which will result in a simpler analysis. In the case of the $^{133}\text{Cs}(n,2n)^{132}\text{Cs}$ reaction, a correction factor of the order of 2% has to be applied in the data, as to correct for the contribution of the $^{133}\text{Cs}(n,a)^{130}\text{I}$ reaction channel on the recorded counting rate.

As a result, the upgrade of the accelerator and the improved beam flux, together with the use of the new detection systems acquired by the INPP, make the conduction of the three aforementioned reactions not only possible, but very promising as well, compared to previous respective measurements. High quality experimental data will result, in previously unexplored energy regions, aiming to provide firm constraints on theoretical estimations and model parameterizations.

- [1] <http://www.inp.demokritos.gr/tandem/> [last visited on 03/2021]
- [2] A. Gandhi, Aman Sharma et al, Measurement of (n,γ) , (n,p) and $(n,2n)$ reaction cross section for sodium, potassium, copper and iodine at neutron energy 14.92 - 0.02 MeV with covariance analysis, *Physical Review C* 102, 014603 (2020).
- [3] Junhua Luo, Li An, Li Jiang, Neutron induced activation cross sections on natural cerium up to 20 MeV, *J Radioanal Nucl Chem* (2015) 305:691–700.
- [4] J. Vrzalova, O. Svoboda et al, Studies of (n,xn) cross-sections in Al, Au, Bi, Cu, Fe, I, In, Mg, Ni, Ta, Y, and Zn by the activation method, *Nuclear Instruments and Methods in Physics Research A* 726(2013)84–90.
- [5] Nobuyuki IWAMOTO, Neutron Nuclear Data Evaluation of Cesium Isotopes for JENDL-4.0, *Journal of Nuclear Science and Technology* (2011), 48:9, 1238-1249.
- [6] PhD, U.O.I. 2021, Efsathia Georgali
- [7] E. Georgali, Z. Eleme, N. Patronis, Study of the $(n,2n)$ reaction on the lightest erbium isotope (^{162}Er) from the reaction threshold up to 19 MeV, *Phys. Rev. C* 98, 014622 (2018)
- [8] E. Georgali, N. Patronis, Experimental study of the $^{165}\text{Ho}(n,2n)$ reaction: Cross section measurements for the population of the ^{164}Ho ground state and isomeric state from the threshold up to 20MeV, *Phys. Rev. C*, 3, 034610 (2020)
- [9] Nuclear reaction experimental data (EXFOR): <https://www.nndc.bnl.gov/exfor/> [last visited on 03/2021]
- [10] K. S. Krane, *Introductory Nuclear Physics*, John Wiley and Sons, 1988.
- [11] G. R. Satchler, *Εισαγωγή στις Πυρηνικές Αντιδράσεις, μετάφραση: Ν. Νικολής, Εκδόσεις Πελεκάνος*
- [12] TALYS User Manual
- [13] G. F. Knoll, *Radiation Detection And Measurement*, John Wiley and Sons, 2000
- [14] G. R. Gilmore, *Practical Gamma-ray Spectrometry*, 2nd Edition, John Wiley & Sons, 2008
- [15] K. Debertin and R. G. Helmer, *Gamma- and X-ray spectrometry with semiconductor detectors*, Elsevier, 1988
- [16] W. R. Leo, *Techniques for Nuclear and Particle Physics Experiments – A how to approach*, Springer-Verlag, 1987
- [17] ROOT User's Guide
- [18] M.Sc. Thesis, U.O.I. 2020, Maria-Elisso Stamati

References and Bibliography

[19] GEANT4 User's Guide: For Application Developers

[20] Agostinelli S. et al, Geant4 – a simulation toolkit, Nucl. Instr. Meth. Phys. Res. A, 506, 3, (2003), 250-303.

[21] Evaluated nuclear data file (ENDF): <https://www.nndc.bnl.gov/exfor/endl00.jsp> [last visited on 02/2021]

[22] National Nuclear Data Center: <https://www.nndc.bnl.gov/nudat2/> [last visited on 03/2021]

DetectorConstructor.cc

```
//=====CANBERRA coaxial HPGe detector (model : GR8023)=====//

#include "XriDetectorConstruction.hh"
#include "XriDetectorMessenger.hh"

#include "G4SDManager.hh"
#include "G4Element.hh"
#include "G4Material.hh"
#include "G4Box.hh"
#include "G4Tubs.hh"
#include "G4Polycone.hh"
#include "G4LogicalVolume.hh"
#include "G4ThreeVector.hh"
#include "G4PVPlacement.hh"
#include "G4NistManager.hh"

#include "G4UnitsTable.hh"
#include "globals.hh"

#include "G4VisAttributes.hh"
#include "G4Colour.hh"

#include "G4SystemOfUnits.hh"
#include "G4PhysicalConstants.hh"
#include "G4RunManager.hh"

XriDetectorConstruction::XriDetectorConstruction():SD(12*cm), gap(6*mm),
outDeadThickness(0.0003*mm), GeCrOutR(78./2.*mm), GeCrHalfh(71.8/2.*mm),
BoreholeOutR(12.5/2.*mm), BoreholeHalfh(62./2.*mm), RingOutR(38/2.*mm),
RingInR(30./2.*mm){
    fMessenger = new XriDetectorMessenger(this);

XriDetectorConstruction::~XriDetectorConstruction(){
    delete fMessenger;}

void XriDetectorConstruction::ConstructSDandField(){}

G4VPhysicalVolume* XriDetectorConstruction::Construct(){

    G4UnitDefinition::BuildUnitsTable();

//=====MATERIALS=====//

// NIST Material definition
G4NistManager* nistManager = G4NistManager::Instance();
```

```

G4Material* Ge = nistManager->FindOrBuildMaterial("G4_Ge");
G4Material* Al = nistManager->FindOrBuildMaterial("G4_Al");
G4Element* eH = nistManager->FindOrBuildElement("H");
G4Element* eC = nistManager->FindOrBuildElement("C");
G4Element* eO = nistManager->FindOrBuildElement("O");

G4Material* Air = nistManager->FindOrBuildMaterial("G4_AIR");
G4Material* Al_salt = nistManager->FindOrBuildMaterial("G4_ALUMINUM_OXIDE");
G4Material* Kapton = nistManager->FindOrBuildMaterial("G4_KAPTON");
G4Material* Mylar = nistManager->FindOrBuildMaterial("G4_MYLAR");

G4double density = 1.3*g/cm3;
G4int ncomponents = 3;
G4int natoms;
G4Material* Epoxy = new G4Material("Epoxy" , density, ncomponents);
Epoxy->AddElement(eH, natoms=44);
Epoxy->AddElement(eC, natoms=15);
Epoxy->AddElement(eO, natoms=7);

density = 0.94*g/cm3;
ncomponents = 2;
G4Material* Hdpe = new G4Material("Hdpe" , density, ncomponents);
Hdpe->AddElement(eH, natoms=4);
Hdpe->AddElement(eC, natoms=2);

G4double pressure, temperature, a;
density = universe_mean_density;
pressure = 3.0E-18*pascal;
temperature = 2.73*kelvin;
G4int z;
G4Material *Vacuum = new G4Material("Vacuum", z=1.0, a=1.01*g/mole,
                                   density, kStateGas, temperature, pressure);

G4cout << "\n\n #####-----##### \n";
G4cout << "\n\n\n\n\t\t ##### List of elements used ##### \n";
G4cout << *(G4Element::GetElementTable());
G4cout << "\n\n\n\n\t\t ##### List of materials used ##### \n";
G4cout << *(G4Material::GetMaterialTable());
G4cout << "\n\n #####-----##### \n";

//=====VOLUMES=====//

//=====beam line along z axis=====//

G4double startFi = 0.0*deg;

```

```
G4double endFi = 360.0*deg;

//=====World Volume=====/

G4double WorldOutR = 30.0*cm;
G4double WorldInR = 0.0*cm;
G4double WorldHalfh = 30.0*cm;

G4Tubs *World_tub
= new G4Tubs("World_tub",WorldInR,WorldOutR,WorldHalfh,
            startFi,endFi);

G4LogicalVolume *World_log
= new G4LogicalVolume(World_tub,Air,"World_log",0,0,0);

G4VPhysicalVolume *World_phys
= new G4PVPlacement(0,G4ThreeVector(),"World",
                    World_log,0,false,0);

//=====Kapton of the source=====/

G4double KaptonOutR = 2.54/2.*cm;
G4double KaptonInR = 0.*cm;
G4double KaptonHalfh = 0.006/2.*cm;

G4Tubs *Kapton_tube
= new G4Tubs("Kapton_tube",KaptonInR, KaptonOutR,KaptonHalfh,
            startFi,endFi);

G4LogicalVolume *Kapton_log
= new G4LogicalVolume(Kapton_tube,Kapton,"Kapton_log",0,0,0);

G4double Pos_x = 0.0*cm;
G4double Pos_y = 0.0*cm;
G4double Pos_z = +KaptonHalfh ;
G4VPhysicalVolume *KaptonTube_phys
= new G4PVPlacement(0,
                    G4ThreeVector(Pos_x,Pos_y,Pos_z),
                    Kapton_log,"KaptonTube",World_log,false,0);

//=====Mylar of the source=====//

G4double MylarOutR = 2.54/2.*cm;
G4double MylarInR = 0.*cm;
G4double MylarHalfh = 0.02539/2.*cm;

G4Tubs *Mylar_tube
```

```
= new G4Tubs("Mylar_tube",MylarInR, MylarOutR,MylarHalfh,
             startFi,endFi);

G4LogicalVolume *Mylar_log
= new G4LogicalVolume(Mylar_tube,Mylar,"Mylar_log",0,0,0);

Pos_x = 0.0*cm;
Pos_y = 0.0*cm;
Pos_z = - MylarHalfh ;
G4VPhysicalVolume *MylarTube_phys
= new G4PVPlacement(0,
                   G4ThreeVector(Pos_x,Pos_y,Pos_z),
                   Mylar_log,"MylarTube",World_log,false,0);

//=====Al of the Mylar=====//

G4double Al_frontOutR = 2.54/2.*cm;
G4double Al_frontInR = 0.*cm;
G4double Al_frontHalfh = 0.00001/2.*cm;

G4Tubs *Al_front_tube
= new G4Tubs("Al_front_tube",Al_frontInR, Al_frontOutR,Al_frontHalfh,
             startFi,endFi);

G4LogicalVolume *Al_front_log
= new G4LogicalVolume(Al_front_tube,Al_salt,"Al_front_log",0,0,0);

Pos_x = 0.0*cm;
Pos_y = 0.0*cm;
Pos_z = - 2*MylarHalfh - Al_frontHalfh ;
G4VPhysicalVolume *Al_frontTube_phys
= new G4PVPlacement(0,
                   G4ThreeVector(Pos_x,Pos_y,Pos_z),
                   Al_front_log,"Al_frontTube",World_log,false,0);

//=====DETECTOR=====//

//=====Vacuum=====//

G4double VacuumOutR = 9.53/2.*cm;
G4double VacuumInR = 0.*cm;
G4double VacuumHalfh = 15./2.*cm;

G4Tubs *Vacuum_tube = new G4Tubs("Vacuum_tube", VacuumInR, VacuumOutR,
VacuumHalfh, startFi, endFi);
```

```
G4LogicalVolume *Vacuum_log = new G4LogicalVolume(Vacuum_tube, Vacuum,
"Vacuum_log", 0, 0, 0);

Pos_x = 0.0*cm;
Pos_y = 0.0*cm;
Pos_z = -SD -VacuumHalfh;

G4VPhysicalVolume *VacuumTube_phys = new G4PVPlacement(0,
G4ThreeVector(Pos_x,Pos_y,Pos_z), Vacuum_log, "VacuumTube", World_log, false, 0);

//=====Carbon Epoxy Entrance window=====//

G4double EpoxyOutR = VacuumOutR;
G4double EpoxyInR = 0.*cm;
G4double EpoxyHalfh = 0.06/2.*cm;

G4Tubs *Epoxy_tube = new G4Tubs("Epoxy_tube", EpoxyInR, EpoxyOutR, EpoxyHalfh,
startFi, endFi);

G4LogicalVolume *Epoxy_log = new G4LogicalVolume(Epoxy_tube, Epoxy, "Epoxy_log", 0, 0,
0);

Pos_x = 0.0*cm;
Pos_y = 0.0*cm;
Pos_z = +VacuumHalfh-EpoxyHalfh;

G4VPhysicalVolume *EpoxyTube_phys = new G4PVPlacement(0,
G4ThreeVector(Pos_x,Pos_y,Pos_z), Epoxy_log, "EpoxyTube", Vacuum_log, false, 0);

//=====Outer Aluminum=====//

G4double AlThickness = 0.15*cm;
G4double AlOutR = EpoxyOutR;
G4double AlInR = AlOutR - AlThickness;
G4double AlHalfh = VacuumHalfh;

G4Tubs *Al_tube = new G4Tubs("Al_tube", AlInR, AlOutR, AlHalfh, startFi, endFi);

G4LogicalVolume *Al_log = new G4LogicalVolume(Al_tube, Al, "Al_log", 0, 0, 0);

Pos_x = 0.0*cm;
Pos_y = 0.0*cm;
Pos_z = 0.0*cm; //-VacuumHalfh-2.*EpoxyHalfh;

G4VPhysicalVolume *AlTube_phys = new G4PVPlacement(0,
G4ThreeVector(Pos_x,Pos_y,Pos_z), Al_log, "AlTube", Vacuum_log, false, 0);
```

```
//=====Holder=====//

G4double HolderHalfh = 9.51/2.*cm;
G4int numZPlanes = 14;
G4double HolderInR[14] = {0.*cm, 0.*cm, 8.2/2.*cm, 8.2/2.*cm, 8.2/2.*cm, 8.2/2.*cm,
8.2/2.*cm, 8.2/2.*cm, 8.2/2.*cm, 8.2/2.*cm, 8.2/2.*cm, 8.2/2.*cm, 8.2/2.*cm, 8.2/2.*cm};
G4double HolderOutR[14] = {8.36/2.*cm, 8.36/2.*cm, 8.36/2.*cm, 8.36/2.*cm, 8.8/2.*cm,
8.8/2.*cm, 8.36/2.*cm, 8.36/2.*cm, 8.8/2.*cm, 8.8/2.*cm, 8.36/2.*cm, 8.36/2.*cm, 8.8/2.*cm,
8.8/2.*cm};
G4double zPlane[14] = {- 9.51*cm, - 9.2*cm, - 9.200001*cm, - 6.00001*cm, - 6.*cm, -
5.1400001*cm, - 5.14*cm, - 2.2600001*cm, - 2.26*cm, - 1.400001*cm, - 1.4*cm, -
0.1300001*cm, - 0.13*cm, 0.*cm};

G4Polycone *Holder_polycone = new G4Polycone("Holder_polycone", startFi, endFi,
numZPlanes, zPlane, HolderInR, HolderOutR);

G4LogicalVolume *Holder_log = new G4LogicalVolume(Holder_polycone, Al, "Holder_log", 0,
0, 0);

Pos_x = 0.0*cm;
Pos_y = 0.0*cm;
Pos_z = (VacuumHalfh - gap);

G4VPhysicalVolume *Holderpolycone_phys = new G4PVPlacement(0,
G4ThreeVector(Pos_x,Pos_y,Pos_z), Holder_log, "Holderpolycone", Vacuum_log, false, 0);

//=====Dead layer=====//

G4double outDeadOutR = GeCrOutR;
G4double outDeadInR = 0.*mm;
G4double outDeadHalfh = GeCrHalfh;

G4Tubs *outDead_tube = new G4Tubs("outDead_tube", outDeadInR, outDeadOutR,
outDeadHalfh, startFi, endFi);

G4LogicalVolume *outDead_log = new G4LogicalVolume(outDead_tube, Ge, "outDead_log", 0,
0, 0);

Pos_x = 0.0*cm;
Pos_y = 0.0*cm;
Pos_z = (VacuumHalfh - outDeadHalfh - gap);

G4VPhysicalVolume *outDeadTube_phys = new G4PVPlacement(0,
G4ThreeVector(Pos_x,Pos_y,Pos_z), outDead_log, "outDeadTube", Vacuum_log, false, 0);

//=====HDPE=====//
```

```
G4double HdpeThickness = 0.01*cm;
G4double HdpeOutR = HdpeThickness + outDeadOutR;
G4double HdpeInR = 0.*mm;
G4double HdpeHalfh = outDeadHalfh + HdpeThickness/2.;

G4Tubs *Hdpe_tube = new G4Tubs("Hdpe_tube", HdpeInR, HdpeOutR, HdpeHalfh, startFi,
endFi);

G4LogicalVolume *Hdpe_log = new G4LogicalVolume(Hdpe_tube, Hdpe, "Hdpe_log", 0, 0, 0);

Pos_x = 0.0*cm;
Pos_y = 0.0*cm;
Pos_z = (VacuumHalfh - HdpeHalfh - gap);

G4VPhysicalVolume *HdpeTube_phys = new G4PVPlacement(0,
G4ThreeVector(Pos_x,Pos_y,Pos_z), Hdpe_log, "HdpeTube", Al_log, false, 0);

//=====Germanium crystal=====//

G4double GeOutR = outDeadOutR - outDeadThickness;
G4double GeInR = 0.*mm;
G4double GeHalfh = outDeadHalfh - outDeadThickness/2.;

G4Tubs *Ge_tube = new G4Tubs("Ge_tube", GeInR, GeOutR, GeHalfh, startFi, endFi);

G4LogicalVolume *Ge_log = new G4LogicalVolume(Ge_tube, Ge, "Ge_log", 0, 0, 0);

Pos_x = 0.0*cm;
Pos_y = 0.0*cm;
Pos_z = 0.0*cm;

G4VPhysicalVolume *GeTube_phys = new G4PVPlacement(0,
G4ThreeVector(Pos_x,Pos_y,Pos_z), Ge_log, "GeTube", outDead_log, false, 0);

//=====Borehole=====//

G4double BoreholeInR = 0.*mm;

G4Tubs *Borehole_tube = new G4Tubs("Borehole_tube", BoreholeInR, BoreholeOutR,
BoreholeHalfh, startFi, endFi);

G4LogicalVolume *Borehole_log = new G4LogicalVolume(Borehole_tube, Vacuum,
"Borehole_log", 0, 0, 0);

Pos_x = 0.0*cm;
Pos_y = 0.0*cm;
Pos_z = (-GeHalfh + BoreholeHalfh);
```

```

G4VPhysicalVolume *BoreholeTube_phys = new G4PVPlacement(0,
G4ThreeVector(Pos_x,Pos_y,Pos_z), Borehole_log, "BoreholeTube", Ge_log, false, 0);

//=====The Ring=====//

G4double RingHalfh = 0.2/2*cm;

G4Tubs *Ring_tube = new G4Tubs("Ring_tube", RingInR, RingOutR, RingHalfh, startFi, endFi);

G4LogicalVolume *Ring_log = new G4LogicalVolume(Ring_tube, Vacuum, "Ring_log", 0, 0, 0);

Pos_x = 0.0*cm;
Pos_y = 0.0*cm;
Pos_z = (-GeHalfh + RingHalfh);

G4VPhysicalVolume *RingTube_phys = new G4PVPlacement(0,
G4ThreeVector(Pos_x,Pos_y,Pos_z), Ring_log, "RingTube", Ge_log, false, 0);

//=====Visualization attributes=====//

World_log->SetVisAttributes (G4VisAttributes::Invisible);
G4VisAttributes *EpoxyTubeAttr = new G4VisAttributes(G4Colour(0.5, 0.5, 0.)); //brown
G4VisAttributes *AlTubeAttr = new G4VisAttributes(G4Colour(1.,0.,0.)); //Red
G4VisAttributes *VacuumTubeAttr = new G4VisAttributes(G4Colour(0.3,0.3,0.3)); //gray
G4VisAttributes *outDeadTubeAttr = new G4VisAttributes(G4Colour(0.,0.8,0.8)); //light gray
G4VisAttributes *HdpeTubeAttr = new G4VisAttributes(G4Colour(1.,0.5,0.)); //orange
G4VisAttributes *GeTubeAttr = new G4VisAttributes(G4Colour(0.,0.4,0.3)); //tale
G4VisAttributes *BoreholeTubeAttr = new G4VisAttributes(G4Colour(0.,0.,1.)); //blue
G4VisAttributes *RingTubeAttr = new G4VisAttributes(G4Colour(0.,0.,1.)); //blue
G4VisAttributes *HolderAttr = new G4VisAttributes(G4Colour(1.,0.,0.)); //Red

G4VisAttributes *MylarTubeAttr = new G4VisAttributes(G4Colour(1.,0.,1.)); //magenta
G4VisAttributes *KaptonTubeAttr = new G4VisAttributes(G4Colour(0.,1.,1.)); //cyan
G4VisAttributes *Al_frontTubeAttr = new G4VisAttributes(G4Colour(0.28, 0.82, 0.8)); //light
blue

MylarTubeAttr->SetVisibility(true);
MylarTubeAttr->SetForceWireframe(true);
Mylar_log->SetVisAttributes(MylarTubeAttr);

HolderAttr->SetVisibility(true);
HolderAttr->SetForceWireframe(true);
Holder_log->SetVisAttributes(HolderAttr);

KaptonTubeAttr->SetVisibility(true);
KaptonTubeAttr->SetForceWireframe(true);
Kapton_log->SetVisAttributes(KaptonTubeAttr);

```

```
Al_frontTubeAttr->SetVisibility(true);
Al_frontTubeAttr->SetForceWireframe(true);
Al_front_log->SetVisAttributes(Al_frontTubeAttr);
```

```
AlTubeAttr->SetVisibility(true);
AlTubeAttr->SetForceWireframe(true);
Al_log->SetVisAttributes(AlTubeAttr);
```

```
VacuumTubeAttr->SetVisibility(true);
VacuumTubeAttr->SetForceWireframe(true);
Vacuum_log->SetVisAttributes(VacuumTubeAttr);
```

```
outDeadTubeAttr->SetVisibility(true);
outDeadTubeAttr->SetForceWireframe(true);
outDead_log->SetVisAttributes(outDeadTubeAttr);
```

```
HdpeTubeAttr->SetVisibility(true);
HdpeTubeAttr->SetForceWireframe(true);
Hdpe_log->SetVisAttributes(HdpeTubeAttr);
```

```
GeTubeAttr->SetVisibility(true);
GeTubeAttr->SetForceWireframe(true);
Ge_log->SetVisAttributes(GeTubeAttr);
```

```
BoreholeTubeAttr->SetVisibility(true);
BoreholeTubeAttr->SetForceWireframe(true);
Borehole_log->SetVisAttributes(BoreholeTubeAttr);
```

```
RingTubeAttr->SetVisibility(true);
RingTubeAttr->SetForceWireframe(true);
Ring_log->SetVisAttributes(RingTubeAttr);
```

```
EpoxyTubeAttr->SetVisibility(true);
EpoxyTubeAttr->SetForceWireframe(true);
Epoxy_log->SetVisAttributes(EpoxyTubeAttr);
```

```
return World_phys;
}
```

```
//=====DetectorMessenger=====//
```

```
void XriDetectorConstruction::UpdateGeometry(){
    G4RunManager::GetRunManager()->DefineWorldVolume(Construct());
    G4RunManager::GetRunManager()->ReinitializeGeometry();
}
```

```
void XriDetectorConstruction::SetOutDeadTh(G4double outDeadThick){
  if (outDeadThickness != outDeadThick) {
    outDeadThickness = outDeadThick;
    UpdateGeometry();
    G4cout << G4endl << "----> Dead layer = " << outDeadThickness << G4endl;
  }
}

void XriDetectorConstruction::SetGap(G4double win_cry_gap){
  if (gap != win_cry_gap) {
    gap = win_cry_gap;
    UpdateGeometry();
    G4cout << G4endl << "----> Gap = " << gap << G4endl;
  }
}

void XriDetectorConstruction::SetSDdist(G4double SDdist){
  if (SD != SDdist) {
    SD = SDdist;
    UpdateGeometry();
    G4cout << G4endl << "----> Source - detector distance = " << SD << G4endl;
  }
}

void XriDetectorConstruction::SetCrystRad(G4double CrysRad){
  if (GeCrOutR != CrysRad) {
    GeCrOutR = CrysRad;
    UpdateGeometry();
    G4cout << G4endl << "----> Crystal Radius = " << GeCrOutR << G4endl;
  }
}

void XriDetectorConstruction::SetCrystHalfh(G4double CrysHalfh){
  if (GeCrHalfh != CrysHalfh) {
    GeCrHalfh = CrysHalfh;
    UpdateGeometry();
    G4cout << G4endl << "----> Crystal Half Length = " << GeCrHalfh << G4endl;
  }
}

void XriDetectorConstruction::SetBorRad(G4double borRad){
  if (BoreholeOutR != borRad) {
    BoreholeOutR = borRad;
    UpdateGeometry();
    G4cout << G4endl << "----> Borehole Radius = " << BoreholeOutR << G4endl;
  }
}
```

```
void XriDetectorConstruction::SetBorHalfh(G4double borHalfh){
  if (BoreholeHalfh != borHalfh) {
    BoreholeHalfh = borHalfh;
    UpdateGeometry();
    G4cout << G4endl << "----> Borehole Half Length = " << BoreholeHalfh << G4endl;
  }
}
```

```
void XriDetectorConstruction::SetRingOutRad(G4double ringOutRad){
  if (RingOutR != ringOutRad) {
    RingOutR = ringOutRad;
    UpdateGeometry();
    G4cout << G4endl << "----> Ring Outer Radius = " << RingOutR << G4endl;
  }
}
```

```
void XriDetectorConstruction::SetRingInRad(G4double ringInRad){
  if (RingInR != ringInRad) {
    RingInR = ringInRad;
    UpdateGeometry();
    G4cout << G4endl << "----> Ring Inner Radius = " << RingInR << G4endl;
  }
}
```


projectile n

element ce

mass 136

ldmodel 1

energy 10 30 1

#---Output---#

channels y

filechannels y

filetotal y

fileresidual y

For a nuclear reaction $a + A \rightarrow C^*$ the production rate of the unstable nuclei N is given by the formula:

$$\frac{dN}{dt} = \sigma \cdot f(t) \cdot N_T - \lambda \cdot N$$

where:

- σ : cross section of the reaction
- $f(t)$: beam flux
- λ : the decay constant of the unstable nuclei

The term $\sigma \cdot f(t) \cdot N_T$ describes the production of the unstable nuclei during the irradiation and the term $-\lambda \cdot N$ describes the simultaneous decay of those nuclei.

Consequently:

$$\frac{dN}{dt} = \sigma \cdot f(t) \cdot N_T - \lambda \cdot N \Leftrightarrow$$

$$\frac{dN}{dt} e^{\lambda t} = \sigma \cdot f(t) \cdot N_T \cdot e^{\lambda t} - \lambda \cdot N \cdot e^{\lambda t} \Leftrightarrow$$

$$\frac{dN}{dt} e^{\lambda t} + N \cdot \lambda \cdot e^{\lambda t} = \frac{dN}{dt} e^{\lambda t} + N \frac{de^{\lambda t}}{dt} = \sigma \cdot f(t) \cdot N_T \cdot e^{\lambda t} \Leftrightarrow$$

$$\frac{d(N \cdot e^{\lambda t})}{dt} = \sigma \cdot f(t) \cdot N_T \cdot e^{\lambda t} \Leftrightarrow$$

$$\int_0^{t_{ir}} \frac{d(N \cdot e^{\lambda t})}{dt} \cdot dt = \int_0^{t_{ir}} \sigma \cdot f(t) \cdot N_T \cdot e^{\lambda t} \cdot dt \Leftrightarrow$$

$$N \cdot e^{\lambda t_{ir}} = \int_0^{t_{ir}} \sigma \cdot f(t) \cdot N_T \cdot e^{\lambda t} \cdot dt + C$$

where:

- $t = 0$: start of the irradiation ($N = 0 \Rightarrow C = 0$)
- t_{ir} : end of irradiation

$$N = \frac{\int_0^{t_{ir}} \sigma \cdot f(t) \cdot N_T \cdot e^{\lambda t} \cdot dt}{e^{\lambda t_{ir}}} = e^{-\lambda t_{ir}} \sigma N_T \int_0^{t_{ir}} f(t) \cdot e^{\lambda t} \cdot dt \Leftrightarrow$$

$$N = e^{-\lambda t_{irr}} \sigma N_T \left(\int_0^{t_{irr}} f(t) \cdot e^{\lambda t} \cdot dt \right) \frac{\int_0^{t_{irr}} f(t) dt}{\int_0^{t_{irr}} f(t) dt} \Leftrightarrow$$

where:

$$\int_0^{t_{irr}} f(t) dt = \Phi \quad \text{: is the total neutron flux}$$

Finally:

$$N = \sigma N_T \Phi f_B \quad \text{where: } f_B = \frac{\int_0^{t_{irr}} f(t) e^{\lambda t} dt}{\int_0^{t_{irr}} f(t) dt} \cdot e^{-\lambda t_{irr}} .$$

The counting rate of the detector is related to the production rate of the nuclei via:

$$\text{counts per second} = \frac{dN}{dt} \cdot \varepsilon \cdot I$$

$$\text{Using } \frac{dN}{dt} = \lambda \cdot N \Leftrightarrow$$

$$\text{counts per second} = \lambda \cdot N \cdot \varepsilon \cdot I .$$

Taking into consideration that $N = N_0 e^{(-\lambda t)}$:

$$\text{counts per second} = \lambda \cdot \varepsilon \cdot I \cdot N_0 \cdot e^{(-\lambda t)} .$$

The total number of counts is obtain by integrating from $t = 0$ until $t = t_m$ when the measurement stops:

$$\text{counts} = \int_0^{t_m} \lambda \cdot \varepsilon \cdot I \cdot N_0 \cdot e^{-\lambda t} \cdot dt = \lambda \cdot \varepsilon \cdot I \cdot N_0 \int_0^{t_m} e^{-\lambda t} \cdot dt = \varepsilon \cdot I \cdot N_0 (1 - e^{-\lambda t_m}) .$$

It is important to note that some nuclei decay immediately after the irradiation before the measurement starts, which corresponds to the waiting time (t_w) discussed earlier in this work, so:

$$N_0 = N e^{-\lambda t_w} \Rightarrow$$

$$\text{counts} = \varepsilon \cdot I (1 - e^{-\lambda t_m}) e^{-\lambda t_w} = \sigma N_T \Phi f_B \varepsilon I (1 - e^{-\lambda t_m}) e^{-\lambda t_w}$$

Finally, the cross section formula that is used in this work is given by:

$$\sigma = \frac{\text{counts}}{\Phi I \varepsilon N_T (1 - e^{-\lambda t_m}) e^{-\lambda t_w} f_B} \quad [6].$$